Pacific Northwest
NATIONAL LABORATORY

PNNL-33932

Rheology of a Wet Waste Feedstock

February 2023

RC Daniel
AJ Schmidt
CA Burns
MR Thorson

U.S. DEPARTMENT OF ENERGY
Prepared for the U.S. Department of Energy
Under contract DE-AC05-76RL01830

DISCLAIMER

PACIFIC NORTHWEST NATIONAL LABORATORY
operated by
BATTELLE
for the
UNITED STATES DEPARTMENT OF ENERGY
under Contract DE-AC05-76RL01830

Printed in the United States of America

Available to DOE and DOE contractors from the Office of Scientific and Technical Information,
P.O. Box 62, Oak Ridge, TN 37831-0062
www.osti.gov
ph: (865) 576-8401
fax: (865) 576-5728
email: reports@osti.gov

Available to the public from the National Technical Information Service
5301 Shawnee Rd., Alexandria, VA 22312
ph: (800) 553-NTIS (6847)
or (703) 605-6000
email: info@ntis.gov
Online ordering: http://www.ntis.gov

PNNL-33932

Rheology of a Wet Waste Feedstock

February 2023

RC Daniel
AJ Schmidt
CA Burns
MR Thorson

Prepared for
the U.S. Department of Energy
Under Contract DE-AC05-76RL01830

Pacific Northwest National Laboratory
Richland, Washington 99354

Acronyms and Abbreviations

EOR	End of run
FOG	Fats, oils, and greases
GLWA	Greater Lakes Water Authority
HTL	Hydrothermal liquefaction
PNNL	Pacific Northwest National Laboratory
RMSE	Root mean square error
TEA	Techno-economic analysis

Contents

Figures

Tables

1.0 Introduction

Hydrothermal liquefaction (HTL) of wet waste feedstocks and subsequent catalytic upgrading of HTL biocrude is being actively developed to enable cost-effective production of renewable fuels (Elliott et al., 2013, 2015, 2017; Snowden-Swan et al., 2017; He et al., 2017; Collett et al., 2019; Zhu et al., 2021a; Thorson et al., 2021; Snowden-Swan et al., 2021, 2022; Cronin et al., 2022). A number of techno-economic analyses (TEAs) have evaluated the impact of HTL feedstock type, including wastewater and sewage sludges, algae, woody, and agriculture residues, and capital equipment on the cost to produce renewable biocrude and fuel blendstocks (Zhu et al., 2014; Snowden-Swan et al., 2016; Jarvis et al., 2018b,a; Zhu et al., 2021b; Li et al., 2021). HTL economics are favored by increased feed solids content, with target solid loadings being 20 % by mass or greater (Snowden-Swan et al., 2016, 2021, 2022). Optimized, cost-effective design of pipelines, pumps, heat-exchangers, vessels, and auxiliary system to transport and heat high-solids slurries to HTL target temperature (up to 360 °C) and pressure (up to 3000 psig) requires estimates of how feed viscosity responds to changes in temperature, solids-loading, and process shear (Snowden-Swan et al., 2022). However, despite evaluation of a diverse array of sanitation and agriculture wastes and opportunistic terrestrial and aquatic feedstocks [e.g., see Elliott et al. (2017), He et al. (2017), Fernandez et al. (2018), Collett et al. (2019), and Zhu et al. (2021a)], the literature provides only limited rheological data for potential HTL feedstocks. As HTL feedstocks typically contain biological materials at high-solids loading, they are expected to be rheologically complex and to exhibit non-Newtonian yield-stress behavior.

The current study provides rheological characterization of a representative HTL feedstock, Wet Waste Feedstock # 22 (WW22), as a function of HTL-prototypic temperature and shear rates. Feed WW22 is derived from a regionally representative blend of food, waste water sludges, and FOG (fats, oils, and greases). Rheological characterization of WW22 as a function of temperature provides, in part, key information for development and economic assessment of HTL wet waste slurry handling and heating operations, which may facilitate improved design rigor and optimization of HTL unit operations. Discussion of WW22 rheology is structured into three separate sections. Section 2.0 discusses WW22 sourcing, base physical and chemical characteristics, and rheometric characterization methods. Section 3.0 details rheometric characterization of WW22 as a function of shear rate, temperature, and solids content, and provides constitutive models and interpolation data by which WW22 rheology may be estimated at HTL-relevant conditions. Finally, Section 4.0 provides a high-level summary of findings regarding WW22 rheology.

2.0 Materials and Methods

The temperature- and shear-dependent stress response of a single HTL feedstock, Wet Waste #22 (WW22), was characterized using an air-bearing rheometer equipped with a high-temperature pressure cell. Rheometric characterization of several WW22 feedstock concentrations spanning 19.4 to 24.8 % (by mass non-volatile solids) enabled evaluation of how temperature- and shear-sensitivities were impacted by solids loading. In the subsections that follow, feedstock sourcing of WW22 is discussed, and the rheometric equipment and measuring approach to used to characterize WW22 rheology are discussed in detail.

2.1 Test Feedstock

Feedstock WW22 is a blend of primary and secondary sludge, food waste, and fats, oils, and greases (FOG) that approximates the average composition of urban wet waste resources in and around Detroit, Michigan (Snowden-Swan et al., 2022). Regional Detroit wastes comprise roughly 33 % sludge, 33 % manure, 9 % FOG, and 25 % food waste by mass (Skaggs et al., 2018; Snowden-Swan et al., 2021). Primary and secondary sludge was sourced from Michigan's Greater Lakes Water Authority (GLWA). Food (kitchen and cafeteria) wastes were sourced from the Coyote Ridge Corrections Central Facility, located in Eastern Washington State. FOG were obtained by collecting decanting floatation scum from primary sludge collected by the Central Contra Costa Sanitary District wastewater treatment and resource recovery facility in California State. Manure wastes were excluded from the WW22 blend to avoid large particle contamination (namely grit, dirt, and straw) typically found in manures, as these contaminants can cause plugging in the small diameter tubing used in the bench-scale HTL system and would have likely done the same in the rheometer geometry used for the current characterization effort. The final blend for WW22 comprised roughly 50 % sludge, 10 % FOG, and 40 % food waste. Table 1, which is adapted from Snowden-Swan et al. (2022), provides a high-level summary of ultimate and proximate analyses for Feed WW22. Five separate WW22 feedstock samples, spanning three solids contents, were prepared for rheometric analysis and are listed in Table 2. Samples WW22-20-A, WW22-25-A, and WW22-25-B were provided for rheometric characterization in early 2021. The solids-contents for these three samples, 19.4 %, 24.8 % and 24.8 %, respectively, were provided upon sample receipt and are reported in Snowden-Swan et al. (2022). Two additional end of run (EOR) WW22 samples were received in mid-2021, WW22-EOR-A and WW22-EOR-B, both with a solids content of 23.3 % by mass. For all samples, solids content was determined gravimetrically by drying the samples at 105 °C until an equilibrium mass was achieved. The solids contents were then calculated as the ratio of dry mass to original wet mass.

2.2 Rheological Characterization Methods

The rheology of WW22 samples was measured using an Anton-Parr MCR301 bench-top rheometer equipped with a 400 bar pressure cell and 300 °C capable heater. Rheology measurements comprised one temperature sweep and three shear-rate sweeps. The specific measuring routine employed for each sample included:

1. a flow curve measurement spanning shear rates from 0 to 1000 s^{-1} at 25 °C,
2. a temperature sweep spanning 25 to 300 °C at a fixed shear rate (sample dependent but ranging from 30 to 150 s^{-1}),
3. a flow curve measurement (again over 0 to 1000 s^{-1}) at 300 °C, and
4. a post temperature treatment flow curve measurement (again over 0 to 1000 s^{-1}) at 25 °C.

For each of the five samples in Table 2, the four steps outlined above were performed on the same sample aliquot (i.e., the sample was not reloaded into the pressure cell between measurements). After the sample was

Table 1. Composition (in weight percent) of WW22 feed inferred from a combination of ultimate and proximate analyses [adapted from Snowden-Swan et al. (2022)].

Analyte	Dry Basis	Dry Ash-Free Basis
From Ultimate Panel Analysis		
C	48.2	55.4
H	7.3	8.4
O	29.1	33.4
N	4.7	5.4
S	0.6	0.7
Ash (Ultimate)	13.5	n/a
P	1.4	n/a
From Proximate Panel Analysis (with carbohydrates by difference)		
Carbohydrate	31.3	36.0
Fat	23.3	26.8
Protein	30.2	34.7
Ash (Proximate)	13.0	n/a
Total Fatty Acid Methyl Ester	16.4	18.9

loaded (but prior to any heating), the sample head-space was purged and filled with high-purity nitrogen to an overpressure of 300 psi. Overpressure was maintained and monitored for leaks for the duration of rheometric characterization and heating to ensure the sample remained in a condensed state. Each flow curve consisted of three segments: an increasing shear rate ramp over 0 to $1000\,s^{-1}$, a shear rate hold at $1000\,s^{-1}$, and a decreasing shear rate ramp from 1000 to $0\,s^{-1}$. The measurement sequence above produces a single temperature sweep at a single shear rate in the range 30-150 s^{-1} for each sample. Multiple temperature sweeps on the sample sample aliquot are not possible because temperature sweep analysis is destructive (i.e., heating of the sample alters the chemical and physical nature of the feedstock and is a natural consequence of the HTL conversion process). While it is nominally possible to re-test a new aliquot of each of the five sample to create a set of temperature sweeps at different shear rates, such testing significantly increases the cost and time required for testing and was foregone in the current characterization effort. As a result, the data set produced by analysis of the five samples does not yield a set of temperature sweep data that may be directly compared against itself due to various combinations of solids content and temperature sweep shear rate.

Shear rate and temperature sweep measurements were controlled and monitored using Anton Paar Rheocompass software. Temperature, shear stress, and shear rate data (denoted by T, τ, and $\dot{\gamma}$, respectively) were collected and exported for post-measurement processing and interpretation. As expected, WW22 feeds exhibited non-Newtonian rheology. Thus, basic characterization of WW2 stress response involved determining the best-fit constitutive parameters using non-Newtonian constitutive equations. The current analysis considers two specific two-parameter constitutive stress-response models:

Table 2. Individual WW22 test samples. Note: EOR stands for "end of run" feed (i.e., unconverted feed leftover after primary HTL testing and described in Snowden-Swan et al. (2021)). A single moisture content was provided for primary and replicate samples.

Sample ID	Description	Solids Content [%]
WW22-20-A	A Nominally 20% Feed	19.4
WW22-EOR-A	WW-22 EOR Feed (Primary)	23.3
WW22-EOR-B	WW-22 EOR Feed (Replicate)	23.3
WW22-25-A	A Nominally 25% Feed (Primary)	24.8
WW22-25-B	A Nominally 25% Feed (Replicate)	24.8

- the Pseudo-plastic equation, which is given by

$$\tau = K_p \dot{\gamma}^{n_p} \tag{1}$$

  where K_p is the plastic consistency and n_p is the plastic flow index, and

- the Casson equation, which is given by

$$\tau = \left(\tau_{c,o}^{\frac{1}{2}} + (K_c \dot{\gamma})^{\frac{1}{2}}\right)^2 \tag{2}$$

  where $\tau_{c,o}$ is the Casson yield stress and K_c is the Casson consistency.

Estimates of the constitutive parameters (K_p, n_p, $\tau_{c,o}$, and K_c) were made using linear least-squares regressions of linearized forms of Eqs. 1 and 2. Neither constitutive model provides a direct means of capturing temperature or solids-content functionality. When evaluating temperature functionalities, a material's rheology is often expressed in terms of its apparent viscosity μ, which is defined by

$$\mu = \frac{\tau}{\dot{\gamma}} \tag{3}$$

For the present analysis, empirical estimates of how apparent viscosity responded to changes in feed temperature were made using:

$$\ln \mu = a + bT + cT^2 + \frac{d}{T} \tag{4}$$

Here, T is temperature (in K) and a, b, c, and d are arbitrary constants selected to fit the observed temperature behavior. Use of the natural logarithm ensures that $\mu > 0$ for all temperatures. Equation 4 is purely empirical and does not explicitly consider the impact of solids loading and the potential for changes in solids content due to material breakdown at high temperature (which is expected for biological feedstocks undergoing thermal conversion). More comprehensive expressions for material stress response (that capture temperature, shear-rate, and solids content) will be developed along-side the results of WW22 flow curve and temperature-sweep measurements in Section 3.0.

Before continuing, it should be noted that only the initial flow curve (at 25 °C) and temperature sweep data are considered in the analyses discussed in this report. Although the measurement protocol outlined above include two additional flow curve measurements of the "heat-treated" feed (one at 300 °C and a second at 25 °C following "heat-treatment"), these data are largely unusable as hydrothermal treatment reduced the feed viscosity below the quantitation limit of the rheometer (of approximately 10 mPa s). In short, the heat-treated materials were too weak to characterize using the pressure-cell rheometer configuration. In practical terms,

handling concerns for HTL feedstocks that fall below the rheometer quantitation limit are negligible, and no additional efforts were made to more accurately measure, quantify, or otherwise model the final rheology of heat-treated materials. Heat-treated sample flow curve measurements are not presented in the main body of the report but may be found in Appendix A.

3.0 Results and Discussion

This report section details rheometric characterization of WW22 as a function of shear-rate, temperature, and solids content. First, the general feedstock stress response as a function of applied shear rate is characterized at ambient temperature (25 °C). In this first characterization, sample baseline flow behavior is interpreted in terms of the Pseudo-Plastic (Eq. 1) and Casson (Eq. 2) constitutive expressions and estimates for the constitutive parameters evaluated using linear regression. Next, the temperature response of WW22 apparent viscosity at several fixed shear rates is evaluated using a simplified temperature expression. After evaluating the temperature behavior, a combination of the Casson expression with expressions for feed yield stress and consistency as a function of both temperature and solid content is used to develop a generalized model for WW22 rheology. Finally, select samples are used to directly evaluate the temperature dependence of the Casson yield stress and consistency. The resulting data and constitutive correlations are then used to develop an apparent viscosity interpolation table (at fixed solids-loading) for use in HTL and other high-temperature feedstock processing designs.

3.1 Characterization of Feedstock Stress Response

Baseline characterization of WW22 stress response was done using the initial three-part flow curve measurement at 25 °C. For each of the five samples, this initial flow curve (item 1 in Section 2.2) comprised an accelerating controlled shear-rate measurement ("up-ramp" data), a fixed shear-rate measurement ("hold" data), and a decelerating shear-rate measurement ("down-ramp" data). An example flow curve for Sample WW22-20-A is provided in Figure 1. Flow curves for the remaining four samples were similar in both their stress response and in the nature of time-dependent behavior (as characterized by the difference between up- and down-ramp shear rate responses, i.e., the flow curve hysteresis) and may be found in Appendix A. In all cases, sample flow curves exhibit hysteresis, with the "up-ramp" stresses being larger than their "down-ramp" stress counterparts at equivalent shear rate. Such hysteresis is indicative of time-dependent breakdown or re-ordering of sample structure due to shear and is typically observed in concentrated slurry stress response. Time-dependent effects are typically limited in extent, lead to a reduction of force needed to shear the sample, and result from the transient build-up of sample structure during initial make-up or quiescent storage.

Figure 2 presents the down-ramp portion of the flow curve measurement for each of the five samples listed in Table 2. These data show excellent reproducibility between primary and replicate samples for WW22-25 and WW22-EOR. All flow curves show significant downward curvature at low-shear rates, meaning that linear constitutive models, i.e., the Newtonian or Bingham-Plastic Equations, are not well-suited for characterizing WW22 stress response.

As noted in Section 2.0, the constitutive behavior of the WW22 feeds was characterized by fitting measured flow curve data to the Pseudo-Plastic (Eq. 1) and Casson (Eq. 2) models. These models are

$$\tau = K_p \dot{\gamma}^{n_p}, \tag{1}$$

and

$$\tau = \left(\tau_{c,o}^{\frac{1}{2}} + (K_c \dot{\gamma})^{\frac{1}{2}}\right)^2 \tag{2}$$

respectively. Both expressions are two parameter models and can accommodate downward curvature, with the Casson expression also able to capture yield stress behavior. Three-parameter (such as the Herschel-Bulkley) and higher order constitutive models were not considered. Determination of WW22 constitutive parameters used the decreasing shear rate portion of the initial 25 °C flow curve (i.e., the data shown in Figure 2). The down ramp data were selected for constitutive characterization because 1) the state of the sample at the end of the three-part flow curve measuring cycle most closely represents the "well-mixed" conditions encountered in process vessels and transfer lines and 2) use of the final measuring condition minimizes history-dependent rheological effects (i.e., sample hysteresis). An example fit of the Pseudo-Plastic and Casson constitutive models

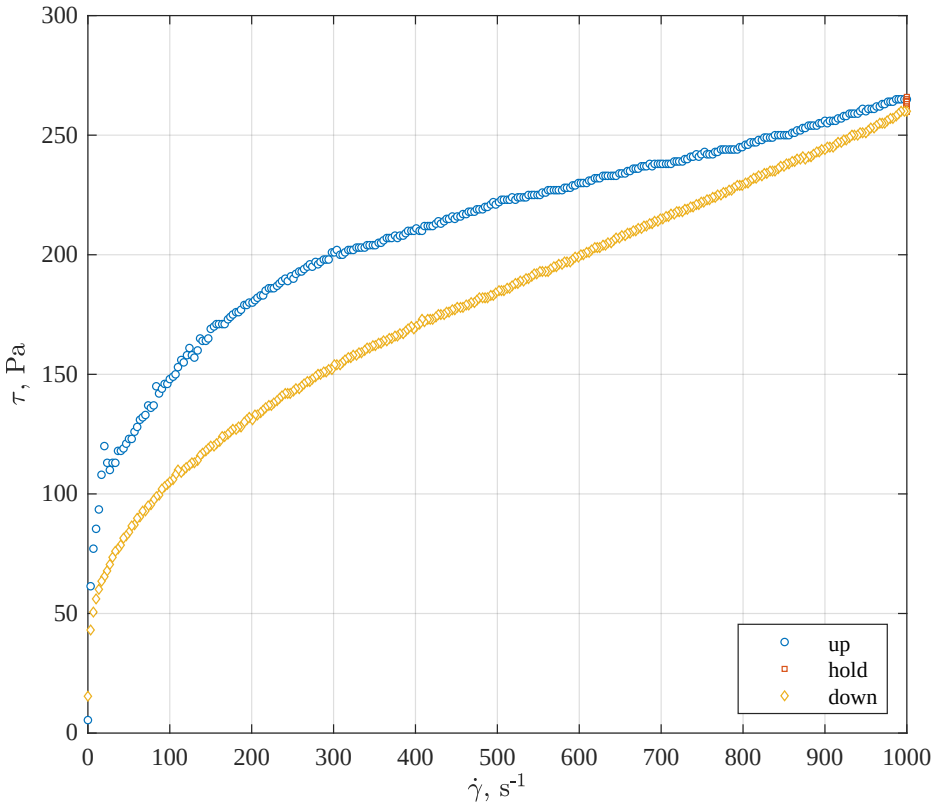

Figure 1. Example three-part flow curve for WW22 Sample WW22-20-A (19.4 % solids). Data correspond to the pre-treatment measuring period at 25 °C.

for Sample WW22-20-A shown in Figure 3. Fits and fit behavior were similar for the four remaining samples (see Appendix A). Table 3 summarizes the best-fit Pseudo-Plastic and Casson parameters for all WW22 feed samples. As demonstrated in Figure 3, the Casson model provides the most accurate constitutive description of the measured flow curves over the entire range of shear rates tested (albeit at the expense of a slight overestimation in yield strength). For this reason, the Casson model was selected to further iterate rheology model functionality with respect to temperature and solids content. This development, is discussed in Section 3.3. However, the temperature functionality of WW22 viscosity is first explored in the section that follows.

3.2 Simple Temperature Model

The temperature dependent rheology behavior for WW22 was characterized through its apparent viscosity. As noted in Section 2.0, apparent viscosity μ is calculated as the ratio of shear stress τ to shear rate $\dot{\gamma}$:

$$\mu = \frac{\tau}{\dot{\gamma}} \tag{3}$$

Initial evaluation of temperature functionality employed the empirical correlation proposed in Section 2.0:

$$\ln \mu = a + bT + cT^2 + \frac{d}{T} \tag{4}$$

Here, T is temperature (in K) and a, b, c, and d are arbitrary constants. Use of the natural logarithm serves to appropriate bound the temperature behavior such that $\mu > 0$ for all temperatures. Equation 4 is empirical (save

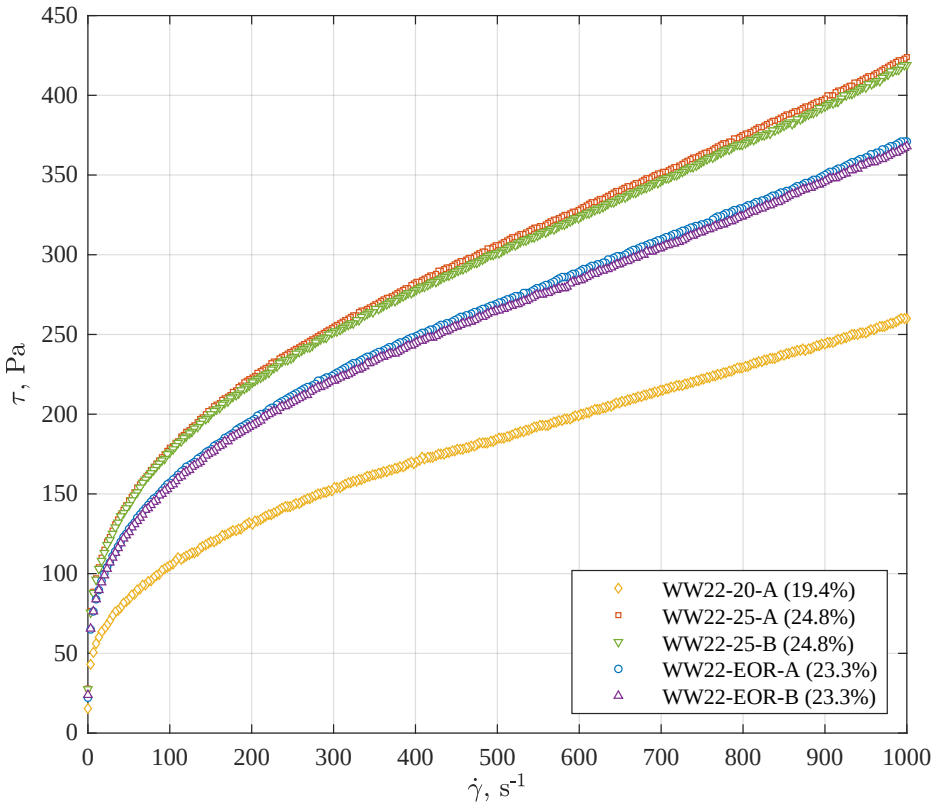

Figure 2. Down ramp flow curve measurements for Table 2 at 25 °C (before heat treatment).

for the T^{-1} term which represents Arrhenian functionality) and does not explicitly consider the impact of solids loading and the potential for changes in solids content due to material breakdown at high temperature (which is expected for biological feedstocks undergoing thermal conversion). For the current report, the temperature sweep data (item 2 in Section 2.2) measured for the five WW22 samples were fit against Eq. 4 using linear regression analysis to determine the best fit values for the temperature coefficients a, b, c, and d. An example fit of the temperature sweep to Eq. 4 is shown in Figure 4 (Sample WW22-20-A). The best fit temperature sweep parameters estimated for all samples are itemized in Table 4. As noted in Section 2.0, each temperature sweep was conducted at a fixed shear rate, and the resulting set of fits presented in Table 4 cannot be readily compared against each other due to a combination of differences in both solids content and temperature sweep shear rate.

The temperature fit shown in Figure 4 follows the general temperature-related decrease in apparent viscosity, but fails to properly capture local variability at both low temperature (25 to 75 °C) and at high temperature (see 160 to 240 °C). And while the quality of fits varies by sample, all fits show deviations like those shown in Figure 4 at high temperature (typically above 160 °C) [see Appendix A]. It is suspected that a combination of lowered viscosity and high-temperature challenges the sensitivity of the magnetically coupled pressure cell rotor and leds to poorer quality measurements at high temperature. While these measurements are expected to bound the measured stress response (i.e., the actual stress response of the material should not exceed that measured), fits above 160 °C should still be approached with caution (i.e., some degree of conservatism should be applied when using the results for estimate and design purposes). Likewise, because Eq. 4 is empirical in nature, extrapolations above and below the temperature range fit here should be treated with similar caution.

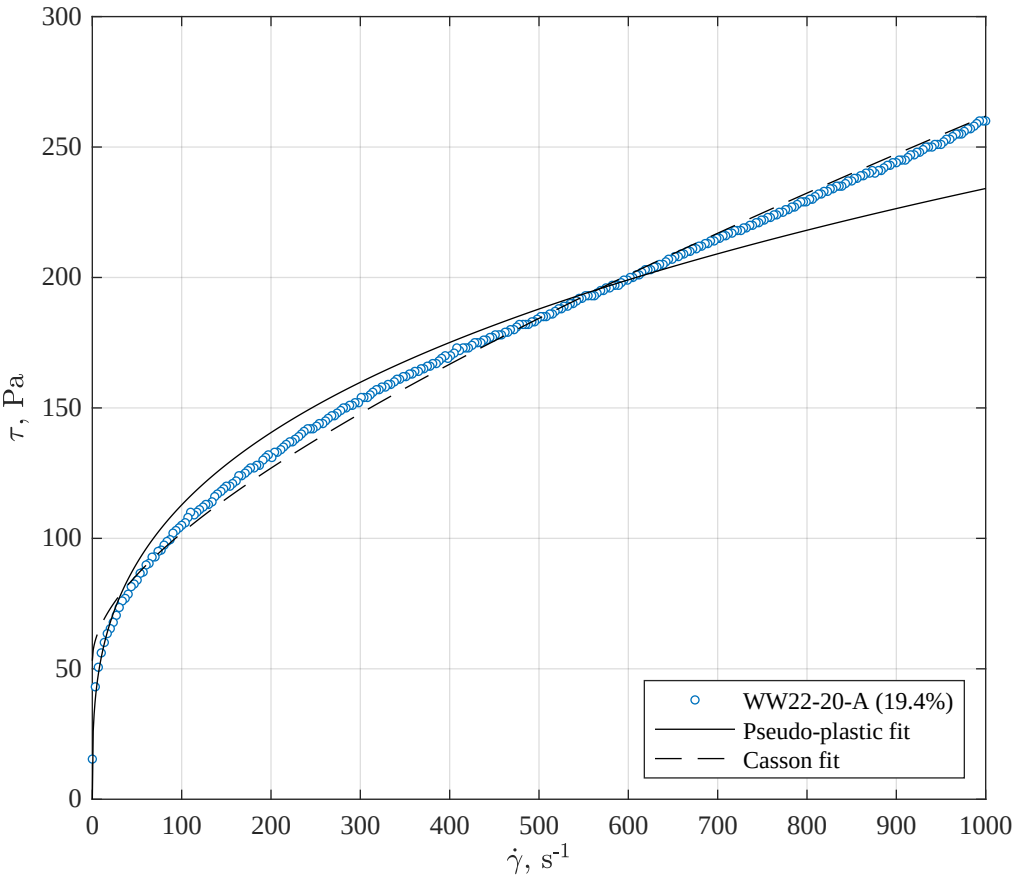

Figure 3. Pseudo-Plastic and Casson fits of the initial (pre-temperature treatment) flow curve data for Sample WW22-20-A (19.4 % solids) at 25 °C. Graph shows the stress response τ as a function of shear rate $\dot{\gamma}$. The solid curve represents the Pseudo-Plastic fit (Eq. 1), whereas the dashed curve represents the Casson fit (Eq. 2). Fitting parameters are given in Table 3.

3.3 Global Correlation

The measurement strategy employed herein (namely the separate flow curve measurements and temperature sweeps) is driven by the difficulty in properly loading, sealing, and running the pressure cell. A typical single measurement takes 4 to 8 h to load the sample, close the cell, and run the set of flow curves and temperature sweeps. The length of time needed to run each measurement, coupled with the potential for leaks (necessitating rerun of the material, as depressurization and exposure to atmosphere at high-temperature rapidly drives off sample moisture), substantially limits the range of solid contents, temperatures, and shear rates that can be evaluated at any given temperature (for flow curves) or shear rate (for temperature sweeps). As such, development of tables that allow interpolation between solid contents, shear rates, and temperatures is limited to the minimal set of measurements that can be reasonably accomplished by the rheologist within the characterization program funding. One such table that facilitates interpolation between select shear rates measured for the WW-22 samples during temperature sweeps shall be provided in the next section. However, there is a general utility in correlations that attempt to account for the combined effects of temperature, solid content, and shear. Because dense feedstock slurry is a complex function of sample shear, temperature, and storage

Table 3. Pseudo-plastic and Casson model constitutive parameters determined by linear-regression of measured data for WW-22 samples against Eqs. 1 and 2. Here, the coefficient of determination (r^2) is provided as a measure of fit quality.

Sample ID	Pseudo-Plastic			Casson		
	K_p, Pas^{-n}	n_p	r^2	$\tau_{c,o}$, Pa	K_c, Pa s	r^2
WW22-20-A	26.2	0.317	0.957	53.1	0.079	0.985
WW22-EOR-A	40.9	0.306	0.966	83.2	0.105	0.980
WW22-EOR-B	41.0	0.303	0.961	82.2	0.103	0.982
WW22-25-A	47.8	0.301	0.959	94.8	0.119	0.983
WW22-25-B	46.9	0.302	0.960	93.4	0.117	0.983

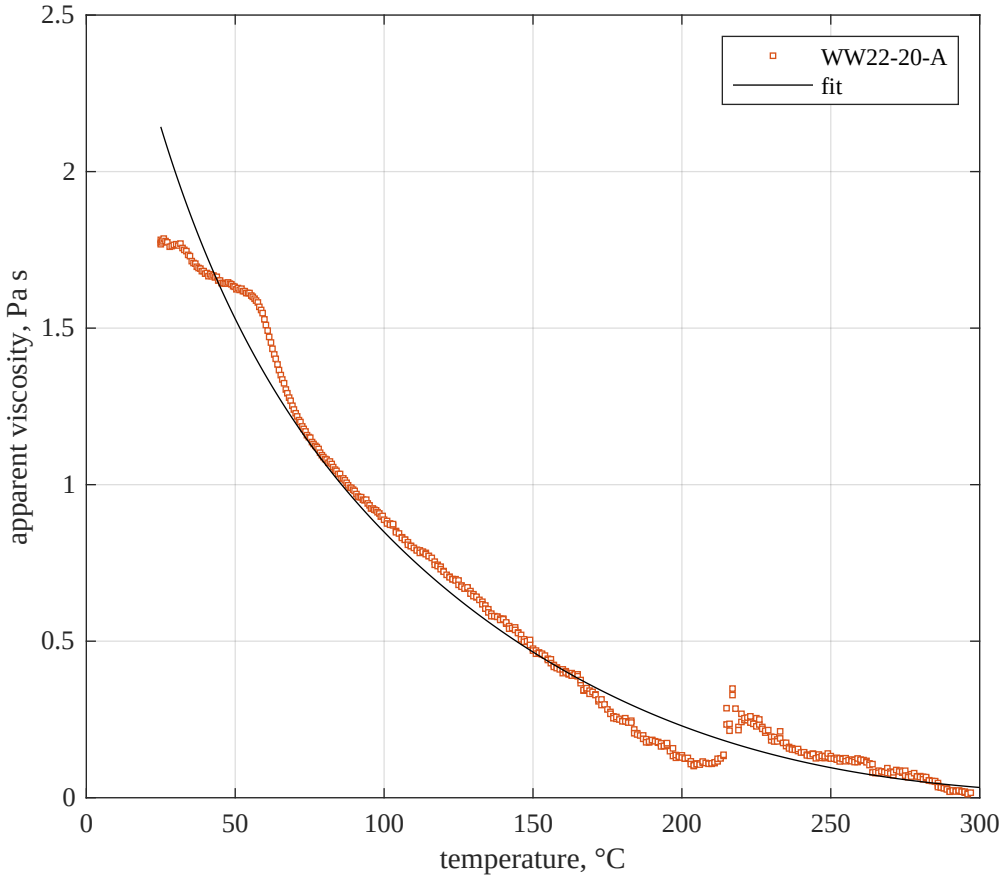

Figure 4. Temperature sweep measurement for WW22-20-A (19.4% solids) at $\dot{\gamma} = 50\,\mathrm{s}^{-1}$. Graph shows the apparent viscosity μ as a function of temperature T.

Table 4. Temperature correlation coefficients for WW-22 samples estimated using the empirical correlation Eq. 4. Coefficients are fit using linear regression for all available temperature data (25 to 300 °C). Measurements, and therefore fit coefficients, are shear rate ($\dot{\gamma}$) specific. Coefficients are such that apparent viscosity μ has units of Pa s and temperature T is in K.

Sample ID	$\dot{\gamma}$, s^{-1}	a	$b \times 10^3$, K^{-1}	$c \times 10^6$, K^{-2}	d, K	r^2
WW22-20-A	50	−20.8	56.7	−62.1	3050	0.943
WW22-EOR-A	30	93.2	−232.0	178.0	−11 400	0.912
WW22-EOR-B	100	−28.6	82.2	−91.5	3840	0.932
WW22-25-A	50	39.5	−94.8	60.8	−4630	0.958
WW22-25-B	150	−30.7	86.9	−95.0	4070	0.975

history, these correlations are highly empirical and subject to greater uncertainty as they do not necessarily capture individual variations in each critical material attribute or process parameter with great accuracy. One limiting factor in crafting correlations and applying them with accuracy is the need to avoid fitting conditions that lead to physically unrealistic constitutive behavior (e.g., negative yield stress and/or consistency).

In the present section, an attempt is made to provide a physically realistic rheology model for WW22 samples that "globally" correlates the combined effects of solids content variation, temperature, and shear rate. Given that samples appear to follow the Casson model, the Casson constitutive equation is a natural starting point for this "global" correlation. Specifically, stress response of the material is assumed to follow:

$$\tau(x,T,\dot{\gamma}) = \left[\left(\tau_{c,o}(x,T)\right)^{\frac{1}{2}} + \left(K_c(x,T)\,\dot{\gamma}\right)^{\frac{1}{2}}\right]^2 \tag{5}$$

where x is the sample solids content at a given temperature T. In Eq. 5, the overall shear rate functionality derives from the Casson equation, whereas the solids content and temperature functionality derive entirely from the constitutive parameters (i.e., consistency and yield stress). The yield stress is assumed to take the form:

$$\tau_{c,o}(x,T) = a_\tau \left(\frac{x_g x^3}{x_g - x}\right) \exp\left[E_\tau\left(\frac{1}{T} - \frac{1}{T_o}\right)\right] \tag{6}$$

where a_τ and E_τ are fitting constants, x_g is the gel concentration of the waste feed material (also fit), and T_o is the reference temperature (specified as 298.15 K). Similarly, the consistency correlation is:

$$K_c(x,T) = \left(a_k x_g\,(x_g - x)^{-\frac{3}{2}} + K_m\right) \exp\left[E_k\left(\frac{1}{T} - \frac{1}{T_o}\right)\right] \tag{7}$$

where a_k and E_k are additional fitting constants and K_m is a minimum sample consistency (set at 1×10^{-5} Pa s). The solids-content functionality presented in Eqs. 6 and 7 have been adapted from Poloski et al. (2006), but have been modified to include Arrhenian temperature functionality. Direct application of these equations using the measured solids contents finds the constitutive parameters decay too slowly relative to actual data. For the present analysis, this slower than measured decay at higher temperatures is attributed to conversion of solids. As an empirical estimate of conversion, the solids content x provided to the constitutive parameter relationships is adjusted from its measured value x_o by:

$$x = x_o\Big(1 - f_c\,F(T)\Big) \quad \text{with} \quad F(T) = \frac{1}{2}\left[1 + \text{erf}\left(\frac{T - T_r}{\sqrt{2}\sigma_r}\right)\right] \tag{8}$$

Here, f_c is the fraction of temperature convertible/degradable solids, T_r is the reaction temperature, and σ_r is the reaction spread. For the present analysis, the reaction temperature and spread were adjusted to manually

comport to the WW22 temperature sweep data and were assigned $T_r = 160\,^{\circ}\mathrm{C}$ and $\sigma_r = 100\,\mathrm{K}$, respectively. The final selected reaction temperature $T_r = 160\,^{\circ}\mathrm{C}$ is reasonable when compared to the range of temperatures at which biological materials start to break down as a result hydrothermal treatment (150 to 300 °C). The fraction convertible feedstock f_c is taken to be the non-ash fraction content of the WW22 feed, which is estimated to be $86.75\,\%$ using the average of the ultimate and proximate ash contents in Table 1. The remaining fitting parameters, namely a_τ, E_τ, a_k, E_k, and x_g, were estimated using non-linear least squares analysis against the global set of pre-temperature sweep flow curve data and temperature sweep data for the five WW22 samples. For the global regression, stress was taken to be the dependent variable while shear rate $\dot{\gamma}$, temperature T, and corrected solids content x were all treated as independent (error-free) variables.

Table 5 presents the best-fit parameters derived from global non-linear regression analysis. Figures 5 through 14 present fits of the pre-temperature sweep flow curves and the temperature sweeps for all samples using the parameters in Table 5 in conjunction with Eqs. 5 through 8. As is expected, the anomalous peaks and excursions observed in the temperature sweep viscosity data are not (and cannot be) properly captured by the assumed Arrhenian temperature functionality. However, outside these localized excursions, the overall quality of the global fits is excellent, and the global predictions agree well with the measured stress and viscosity data. The root mean square error of the fit is $5.61\,\mathrm{Pa}$. As such, the model should be a suitable means of estimating WW22 rheology within the bounds of temperature (25 to 300 °C), solids content (19.4 to 24.8 %), and shear rate (0 to $1000\,\mathrm{s}^{-1}$) evaluated for the five feed samples.

The overall "quality" of the fit may also be judged by evaluating the reasonableness of the regressed model parameters (namely, a_τ, a_k, E_τ, E_k, and x_g). Because parameters a_τ and a_k are pre-factors to functions of solids contents, their immediate interpretation is difficult without specifying a fixed solids content. For this reason, the reasonableness of a_τ and a_k are best judged by evaluating $\tau_{c,o}$ and K_c at a reference solids content temperature. Using $x_o = 24\,\%$ and $T = T_o$ (i.e., $25\,^{\circ}\mathrm{C}$), $\tau_{c,o} \simeq 98\,\mathrm{Pa}$ and $K_c \simeq 96\,\mathrm{mPa\,s}$. Both $\tau_{c,o}$ and K_c estimates seem reasonable with respect to the Casson parameters reported for the WW22-25 and -EOR samples (which most closely correspond to the selected solids content $x_o = 24\,\%$) in Table 3, although the global yield stress is somewhat larger and the consistency somewhat lower than those estimated from linear-regression of the ambient temperature flow curve data. The activation energies, E_τ and E_k, estimated using the global correlation are modest. Typical activation energies found for liquid viscosity are on the order of $1000\,\mathrm{K}$ [e.g., analysis of concentrated salt solutions activation energies find $E_k \simeq 2000\,\mathrm{K}$ — see Daniel et al. (2009)]. That the yield stress activation energy ($\sim$400 K) is lower than that for consistency is indicative that yield stress is less sensitive to changes in temperature (for a given solids loading). Finally, analysis indicates a gel concentration of $x_g = \sim 93\,\%$. This gel content is much larger than anticipated for the system and would appear to suggest the possibility for significant consolidation of WW22 solids. However, material consolidation to $\sim 90\,\%$ is physically unrealistic, at least with respect to other biological feedstocks which typically consolidate to maximum packings of approximately $\sim 30\,\%$. It is more likely that the inferred gel concentration $x_g = 0.93$ reflects the semi-empirical nature of the global correlation or indicates that the overall fraction of solids in the feed does not accurately represent the content of material that fundamentally controls feed rheology.

Table 5. Best-fit global rheology model parameters as determined by non-linear regression analysis. Non-linear regression is effected by minimizing the error in the measured stress at a given temperature, shear rate, and solids content. Various measures of the quality of the fit are given below, including the standard error of the coefficients (the "Error"), the coefficient of determination r^2, and the root mean square error (RMSE).

Parameter	Unit	Value	Error
a_τ	Pa	6880	47
E_τ	K	400	17
a_k	Pa s	0.0640	0.000 50
E_k	K	1090	47
x_g	– –	0.928	0.015
r^2 (Adjusted)	– –	0.995	– –
RMSE	Pa	5.61	– –

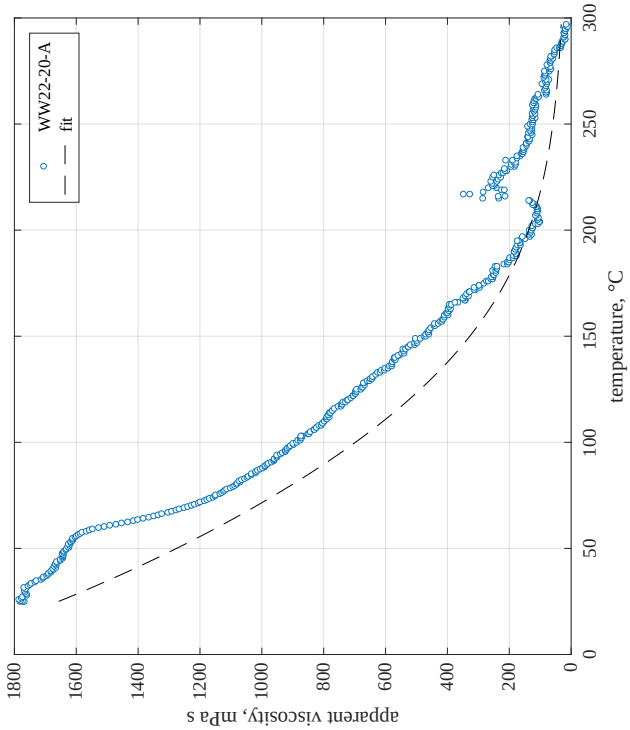

Figure 6. Global fit of the WW22-20-A temperature sweep at $\dot{\gamma} = 50\,\mathrm{s}^{-1}$.

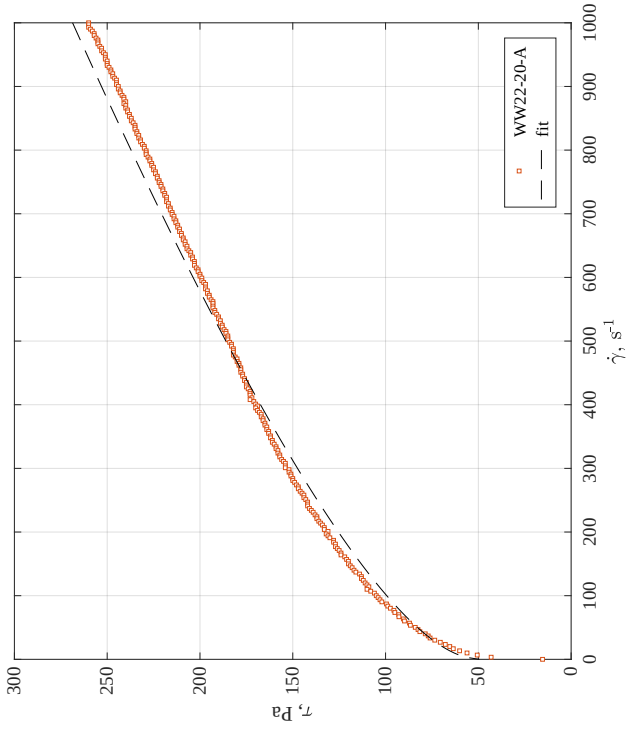

Figure 5. Global fit of the 25 °C pre-temperature sweep flow curve for WW22-20-A.

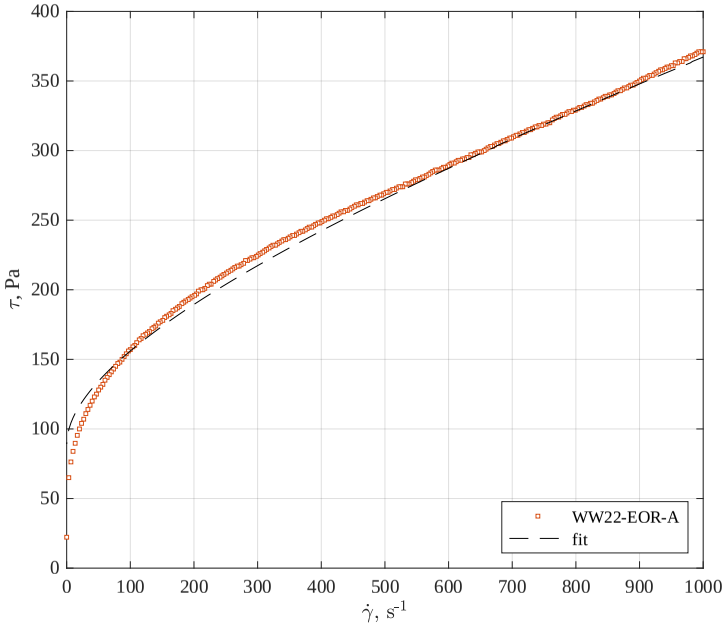

Figure 7. Global fit of the 25 °C pre-temperature sweep flow curve for WW22-EOR-A.

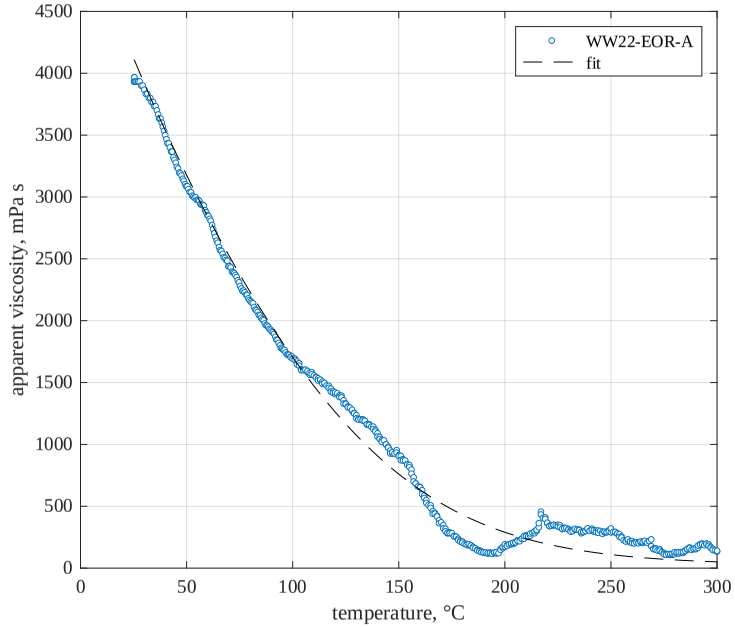

Figure 8. Global fit of the WW22-EOR-A temperature sweep at $\dot{\gamma} = 30\,\mathrm{s}^{-1}$.

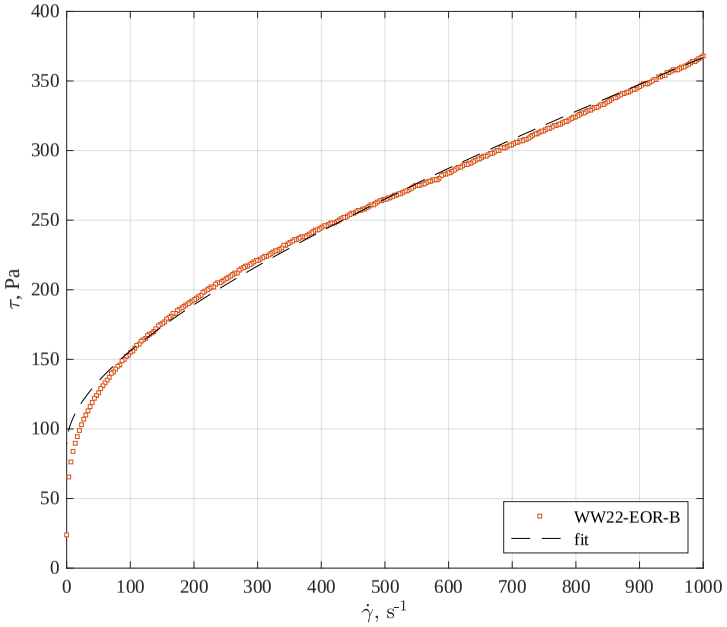

Figure 9. Global fit of the 25 °C pre-temperature sweep flow curve for WW22-EOR-B.

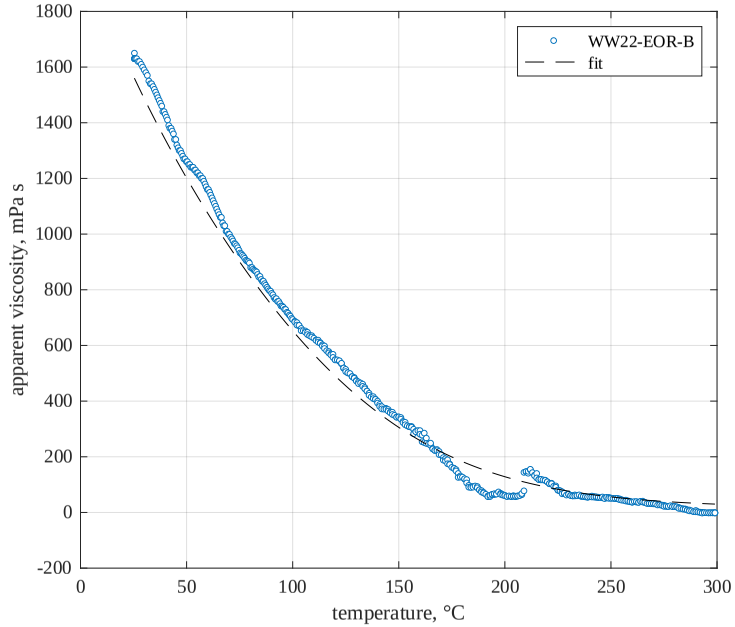

Figure 10. Global fit of the WW22-EOR-B temperature sweep at $\dot{\gamma} = 100\,\mathrm{s}^{-1}$.

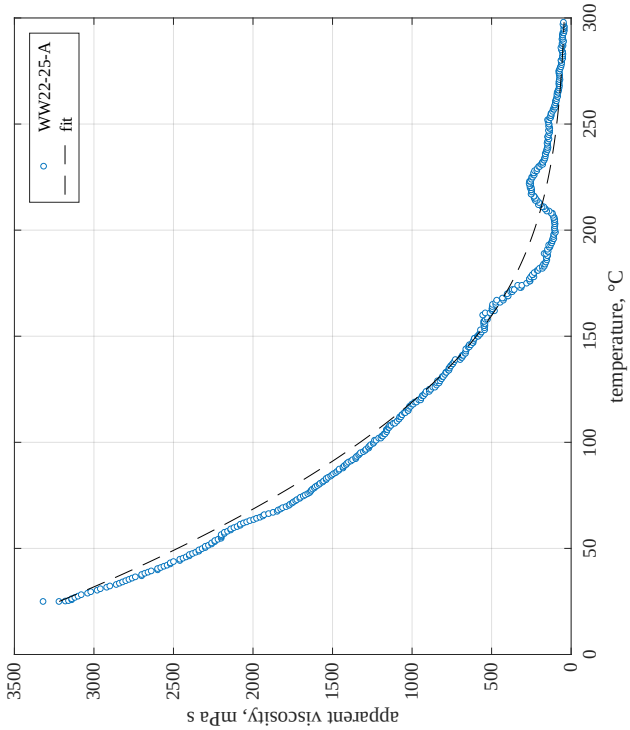

Figure 12. Global fit of the WW22-25-A temperature sweep at $\dot{\gamma} = 50\,\mathrm{s}^{-1}$.

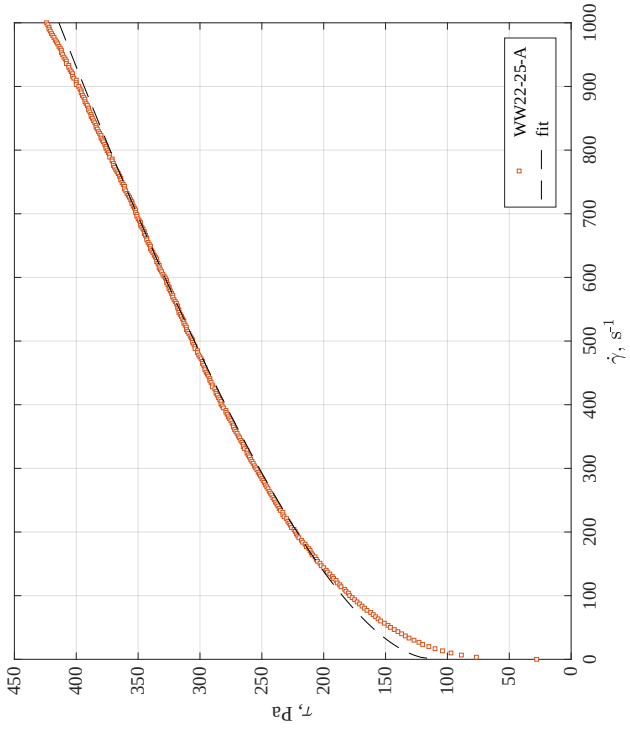

Figure 11. Global fit of the 25 °C pre-temperature sweep flow curve for WW22-25-A.

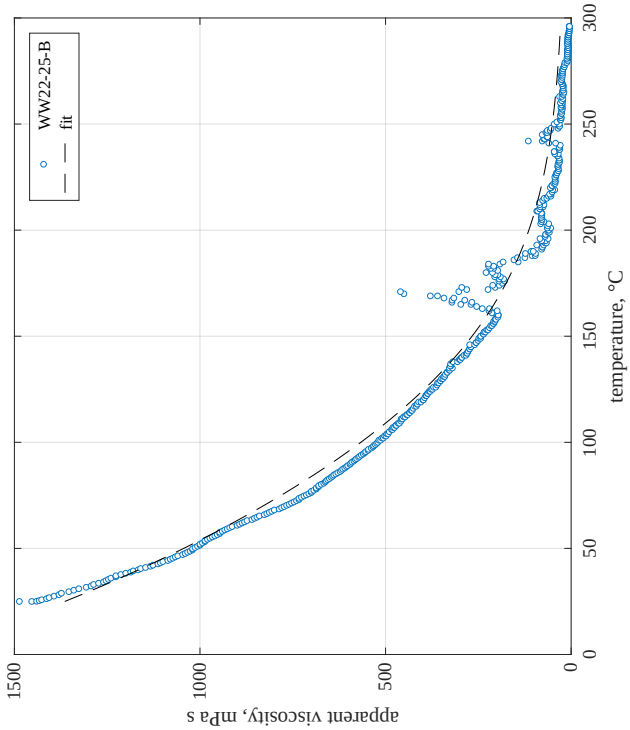

Figure 14. Global fit of the WW22-25-B temperature sweep at $\dot{\gamma} = 150\,\mathrm{s}^{-1}$.

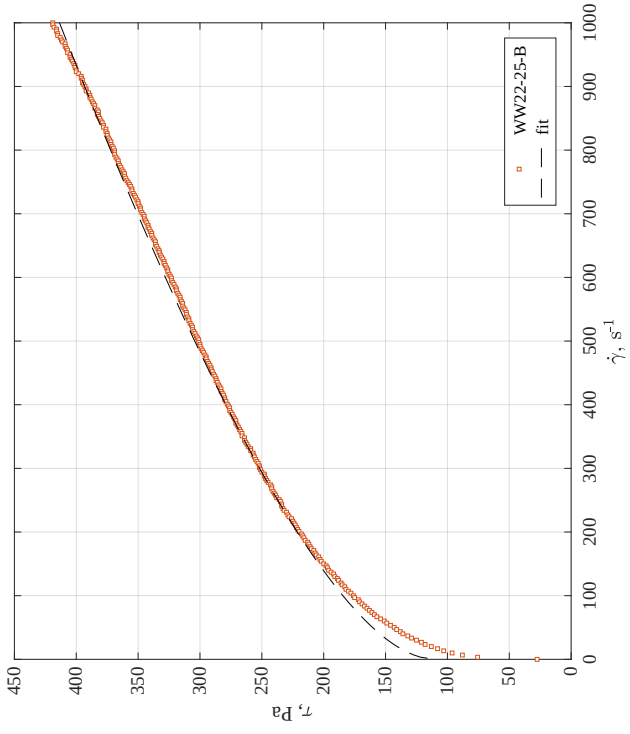

Figure 13. Global fit of the 25 °C pre-temperature sweep flow curve for WW22-25-B.

3.4 Interpolation Table

Engineering analyses may seek to use the raw data to interpolate the specific temperature behavior of feed WW-22 rather than relying on the correlations developed in the preceding sections. Interpolation allows incorporation of the excursions observed in the temperature profiles but not faithfully captured in the simplified temperature or global correlations. Table 6 provides an interpolation table for WW-22 feed apparent viscosity as a function of temperature and shear rate. To minimize the impact of solid content variations in the samples, only WW22-25 and WW22-EOR samples have been incorporated into the table. This renders the table applicable to only WW22 feeds with solids contents around 23 to 25 % (or 24 ± 1 %). Despite the variability in solids content (and the accompanying variability in viscosity it introduces), interpolated viscosities provide a more accurate representation of the low-shear measurement conditions and localized viscosity excursions that result from high-temperature conversion.

As a final analysis, the data presented in Table 6 were used to estimate the temperature specific Casson parameters ($\tau_{c,o}$ and K_c) at low shear rate (30 to 150 s^{-1}) via linear least squares analysis. Specifically, the nominally four interpolated viscosities provided for each temperature in Table 6 were fit to a linearized form of the Casson apparent viscosity expression, namely,

$$\mu^{\frac{1}{2}} = \tau_{c,o}^{\frac{1}{2}} \dot{\gamma}^{-\frac{1}{2}} + K_c^{\frac{1}{2}} \tag{9}$$

The results of this analysis are shown in Figure 15, which plots the Casson constitutive parameters (yield stress $\tau_{c,o}$ — blue points, left-hand axis; consistency K_c — orange points, right-hand axis) as a function of temperature for WW22 at a nominal solids content of 24 ± 1 %. Also shown on Figure 15 are the Casson yield stress and consistency predictions (blue and orange dashed lines) made using the global fit correlations, namely Eqs. 6 and 7, respectively, at $x_o = 24$ %. In general, the Casson yield stress derived from fits of low shear rate data to Eq. 9 approximates that predicted by the global correlation, whereas the low shear rate derived consistencies vary more significantly as a function of temperature relative to those predicted by the global correlation. With respect to yield stress, the global predictions generally fall above those inferred via Eq. 9, which seems reasonable given the tendency of the Casson model to over-predict stress at low shear rates (see the Casson fit over the 0 to 100 s^{-1} in Figure 13). And given the slight "over-prediction" in yield stress by the global correlation relative to those derived from Eq. 9, the corresponding "under-prediction" of the global consistency correlation is expected to a certain extent in that it is needed to balance yield stress when approximating the material stress response τ (i.e., the fit objective). Overall, the given the combination of disparate solids contents and the limited shear rate used to derive the Figure 15 results, the differences between these results and those predicted by the global correlation are sensible and reflect the difficulty in fitting complex feedstock rheology using a single, global correlation.

As a final note, Figure 15 omits results producing negative values of $\tau_{c,o}^{1/2}$ and $K_c^{1/2}$ and regressions where $r^2 \leq 0.75$. These restrictions general eliminate estimates of $\tau_{c,o}$ and K_c above 160 °C, suggesting the quality of the stress response data are reduced at high temperatures and prevent meaningful determination of constitutive parameters above 160 °C. Loss of correlation at temperatures above 160 °C aligns with previous arguments that the breakdown of biological material (and corresponding reduction in solids content) occurs at $T_r = 160$ °C (see Eq. 8). Moreover, the loss of correlation at temperature above 160 °C underscores the importance of handling WW22 high-temperature data (i.e., any data measured at temperatures >160 °C) and correlations derived therefrom with caution. While it is expected that the stress response estimated at these conditions bounds the actual stress response of the material, designs employing these data should employ additional conservatism to ensure the inherent uncertainties are properly accommodated.

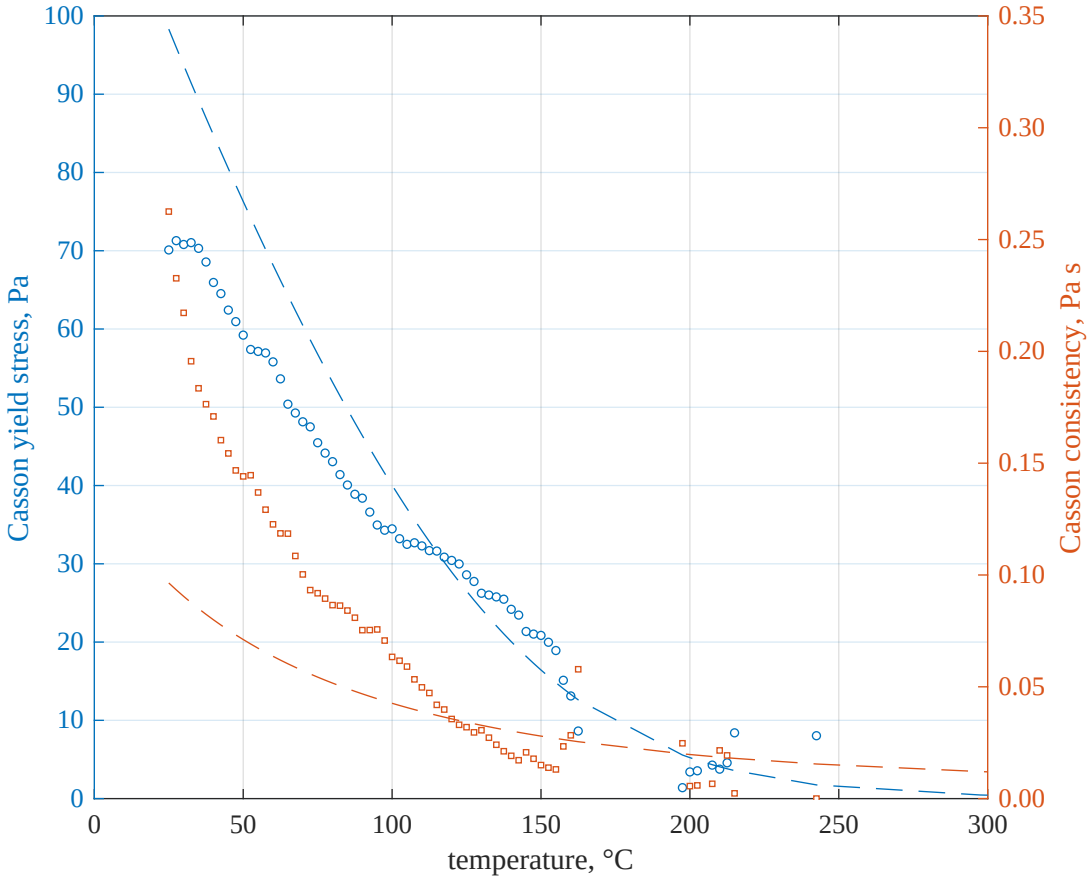

Figure 15. Estimates of Casson yield stress (blue circles) and consistency (red square) as a function of temperature. Evaluation of the constitutive parameters uses the interpolation data provided in Table 6 via linear regression. Parameters are specific to WW22 feeds at approximately $24 \pm 1\,\%$ (by mass). Linear regressions producing negative values for $\tau_{c,o}^{1/2}$ and $K_c^{1/2}$ have been omitted. Additionally, analyses yielding $r^2 \leq 0.75$ have been similarly omitted. The dashed lines represent Casson yield stress (blue) and consistency (red) predictions using global correlation Eqs. 6 and 7, respectively, and Table 5 parameter estimates.

Table 6. Interpolation table for WW22 feed viscosity at approximately $24 \pm 1\,\%$.

Temperature, °C	Apparent Viscosity μ, Pa s			
	$\dot{\gamma} = 30\,\mathrm{s}^{-1}$	$\dot{\gamma} = 50\,\mathrm{s}^{-1}$	$\dot{\gamma} = 100\,\mathrm{s}^{-1}$	$\dot{\gamma} = 150\,\mathrm{s}^{-1}$
25.0	3.9621	3.2505	1.6399	1.4618
27.5	3.9328	3.1039	1.6202	1.3947
30.0	3.8669	2.9952	1.5914	1.3463
32.5	3.8011	2.8885	1.5495	1.2921
35.0	3.7337	2.7903	1.5172	1.2516
37.5	3.6339	2.7047	1.4721	1.2157
40.0	3.4956	2.6113	1.4261	1.1664
42.5	3.3841	2.5326	1.3799	1.1182
45.0	3.2678	2.4517	1.3315	1.0797
47.5	3.1705	2.3801	1.2891	1.0425
50.0	3.0884	2.3162	1.2606	1.0150
52.5	3.0188	2.2578	1.2406	0.9952
55.0	2.9790	2.2083	1.2211	0.9703
57.5	2.9313	2.1760	1.1965	0.9454
60.0	2.8559	2.1121	1.1615	0.9159
62.5	2.7434	2.0392	1.1207	0.8791
65.0	2.6074	1.9501	1.0772	0.8418
67.5	2.5247	1.8601	1.0331	0.8058
70.0	2.4429	1.7850	0.9977	0.7693
72.5	2.3828	1.7342	0.9697	0.7415
75.0	2.2914	1.6744	0.9374	0.7156
77.5	2.2224	1.6313	0.9131	0.6928
80.0	2.1635	1.5884	0.8875	0.6740
82.5	2.0931	1.5438	0.8651	0.6546
85.0	2.0288	1.4963	0.8400	0.6346
87.5	1.9651	1.4490	0.8140	0.6132
90.0	1.9199	1.4079	0.7876	0.5946
92.5	1.8467	1.3605	0.7626	0.5761
95.0	1.7775	1.3195	0.7417	0.5575
97.5	1.7292	1.2750	0.7181	0.5374

Table 6. Interpolation table for WW22 feeds, cont'd.

Temperature, °C	Apparent Viscosity μ, Pa s			
	$\dot{\gamma} = 30\,\mathrm{s}^{-1}$	$\dot{\gamma} = 50\,\mathrm{s}^{-1}$	$\dot{\gamma} = 100\,\mathrm{s}^{-1}$	$\dot{\gamma} = 150\,\mathrm{s}^{-1}$
100.0	1.7029	1.2436	0.6943	0.5214
102.5	1.6472	1.1950	0.6727	0.5043
105.0	1.6040	1.1650	0.6538	0.4895
107.5	1.5834	1.1406	0.6398	0.4738
110.0	1.5579	1.0973	0.6257	0.4606
112.5	1.5209	1.0666	0.6118	0.4455
115.0	1.4938	1.0304	0.5924	0.4300
117.5	1.4492	1.0030	0.5710	0.4172
120.0	1.4157	0.9563	0.5535	0.3999
122.5	1.3861	0.9247	0.5372	0.3886
125.0	1.3265	0.8838	0.5106	0.3750
127.5	1.2830	0.8429	0.4922	0.3594
130.0	1.2248	0.8180	0.4739	0.3479
132.5	1.1981	0.7887	0.4599	0.3343
135.0	1.1702	0.7651	0.4349	0.3270
137.5	1.1402	0.7395	0.4155	0.3160
140.0	1.0763	0.6925	0.3950	0.2936
142.5	1.0307	0.6665	0.3754	0.2790
145.0	0.9690	0.6448	0.3662	0.2699
147.5	0.9364	0.6185	0.3522	0.2548
150.0	0.9129	0.5897	0.3406	0.2418
152.5	0.8717	0.5598	0.3243	0.2296
155.0	0.8145	0.5447	0.3062	0.2139
157.5	0.7077	0.5448	0.2959	0.2060
160.0	0.6394	0.5342	0.2810	0.1968
162.5	0.5628	0.5015	0.2620	0.2281
165.0	0.4830	0.4777	0.2403	0.2701
167.5	0.4279	0.4358	0.2229	0.3308
170.0	0.3569	0.3893	0.2056	0.3829
172.5	0.2999	0.3469	0.1835	0.2727
175.0	0.2721	0.2840	0.1667	0.1783

Table 6. Interpolation table for WW22 feeds, cont'd.

Temperature, °C	Apparent Viscosity μ, Pa s			
	$\dot{\gamma} = 30\,\mathrm{s}^{-1}$	$\dot{\gamma} = 50\,\mathrm{s}^{-1}$	$\dot{\gamma} = 100\,\mathrm{s}^{-1}$	$\dot{\gamma} = 150\,\mathrm{s}^{-1}$
177.5	0.2432	0.2517	0.1422	0.1977
180.0	0.2068	0.2276	0.1244	0.2082
182.5	0.1910	0.1844	0.1046	0.2154
185.0	0.1700	0.1585	0.0900	0.1750
187.5	0.1427	0.1543	0.0885	0.1187
190.0	0.1272	0.1519	0.0681	0.0981
192.5	0.1220	0.1343	0.0604	0.0781
195.0	0.1207	0.1189	0.0654	0.0730
197.5	0.1396	0.1072	0.0690	0.0692
200.0	0.1797	0.1024	0.0599	0.0595
202.5	0.1923	0.1031	0.0585	0.0671
205.0	0.2097	0.1046	0.0564	0.0792
207.5	0.2315	0.1193	0.0676	0.0812
210.0	0.2575	0.1618	0.1342	0.0853
212.5	0.2683	0.2022	0.1513	0.0788
215.0	0.3177	0.2278	0.1261	0.0696
217.5	0.4194	0.2479	0.1176	0.0513
220.0	0.3716	0.2538	0.1104	0.0515
222.5	0.3393	0.2587	0.0990	0.0456
225.0	0.3478	0.2443	0.0835	0.0416
227.5	0.3199	0.2272	0.0690	0.0374
230.0	0.3146	0.2006	0.0639	0.0342
232.5	0.3053	0.1728	0.0602	0.0329
235.0	0.3084	0.1638	0.0610	0.0355
237.5	0.2926	0.1540	0.0566	0.0393
240.0	0.3181	0.1470	0.0560	0.0352
242.5	0.2977	0.1459	0.0561	0.0828
245.0	0.2938	0.1408	0.0534	0.0648
247.5	0.2899	0.1363	0.0528	0.0549
250.0	0.3029	0.1410	0.0516	0.0314
252.5	0.2853	0.1387	0.0497	0.0312

Table 6. Interpolation table for WW22 feeds, cont'd.

Temperature, °C	Apparent Viscosity μ, Pa s			
	$\dot{\gamma} = 30\,\mathrm{s}^{-1}$	$\dot{\gamma} = 50\,\mathrm{s}^{-1}$	$\dot{\gamma} = 100\,\mathrm{s}^{-1}$	$\dot{\gamma} = 150\,\mathrm{s}^{-1}$
255.0	0.2480	0.1222	0.0456	0.0253
257.5	0.2204	0.1077	0.0415	0.0256
260.0	0.2109	0.0977	0.0380	0.0249
262.5	0.2055	0.0904	0.0377	0.0251
265.0	0.2104	0.0843	0.0385	0.0222
267.5	0.2193	0.0754	0.0323	0.0214
270.0	0.1698	0.0755	0.0318	0.0258
272.5	0.1422	0.0712	0.0279	0.0249
275.0	0.1209	0.0762	0.0243	0.0232
277.5	0.1074	0.0629	0.0217	0.0184
280.0	0.1205	0.0610	0.0215	0.0111
282.5	0.1245	0.0509	0.0152	0.0101
285.0	0.1400	0.0597	0.0116	0.0093
287.5	0.1603	0.0542	0.0059	0.0091
290.0	0.1575	0.0526	0.0036	0.0093
292.5	0.1942	0.0521	– –	0.0067
295.0	0.1926	0.0427	– –	0.0049
297.5	0.1618	0.0494	– –	– –
300.0	0.1374	– –	– –	– –

4.0 Conclusions

In the present report, the rheology of a wet waste HTL feedstock was characterized as a function of temperature over 25 to 300 °C and solids content using a high-pressure, high-temperature rheometer. The feed characterized, Wet Waste Feedstock #22 (WW2), is a blend of waste water sludges, food wastes, and fats, oils, and greases (FOG) that approximates the average composition of urban wet wastes generated in and around Detroit, Michigan. Five WW22 samples2, spanning three unique solids contents of 19.4 %, 23.3 %, and 24.8 % (by mass), were evaluated at ambient temperature (to determine their stress response with respect to variable shear rate) and as a function of temperature at fixed shear rate. Evaluation of the ambient constitutive behavior of WW22 feed samples suggests it is yield stress fluid whose behavior can be well-approximated using the Casson two-parameter constitutive equation. The temperature sweep data for each sample were correlated using a semi-empirical temperature expression. Likewise, a "global" correlation was used to capture the combined effects of solids content, shear rate, and temperature using data from each of the five samples into a single, general-use model. The global correlation used the Casson constitutive equation to account for the impact of shear; functional forms for Casson yield stress and consistency were proposed and fit to account for the individual effects that solids content and temperature had on material stress response. Global model coefficients were estimated using a combination of reasonable inference and non-linear regression analysis. The final model and model parameters showed reasonable correlation to the measured data, with an r^2 (coefficient of determination) value of 0.995 and an root mean square error of 5.61 Pa. Accompanying this model is a separate analysis that uses the temperature sweep data to evaluate the functionality of Casson yield stress and consistency as a function of temperature. As the latter relies on low shear temperature sweep data (which is limited to fixed shear rates over 30 to 150 s^{-1}), the "secondary" Casson yield stress and consistency estimates differ from those predicted using the global correlation (which are based on data including both the temperature sweeps and full-shear ambient characterization spanning 0 to 1000 s^{-1} data). The differences in the secondary and global Casson parameters appear to be a natural result of the differences in source data, and are such that the differences will be negated when evaluating stress, at least within the limits of how well the Casson model generally fits the source rheology data. Overall, the results presented herein provide suitable data (including raw rheology measurements, rheology correlations, and viscosity interpolation tables) to aid in the design of robust HTL feedstock handling systems.

5.0 References

Collett JR, JM Billing, PA Meyer, AJ Schmidt, A Remington, ER Hawley, BA Hofstad, EA Panisko, Z Dai, TR Hart, DM Santosa, JK Magnuson, RT Hallen, and SB Jones. 2019. "Renewable Diesel via Hydrothermal Liquefaction of Oleaginous Yeast and Residual Lignin from Bioconversion of Corn Stover." *Applied Energy* 233–234:840–853.

Cronin DJ, AJ Schmidt, JM Billing, TR Hart, SP Fox, XF Almansa, JW Norton, and MR Thorson. 2022. "Comparative Study on the Continuous Flow Hydrothermal Liquefaction of Various Wet-Waste Feedstock Types." *ACS Sustainable Chemical Engineering* 10:1256–1266.

Daniel RC, JM Billing, ML Bonebrake, KJ Cantrell, LK Jagoda, ML Luna, RA Peterson, and RW Shimskey. 2009. *Characterization of Filtration Scale-Up Performance*. PNNL-18117 (WTP-RPT-168, Rev. 0), Pacific Northwest National Laboratory, Richland, WA, United States.

Elliott DC, P Biller, AB Ross, AJ Schmidt, and SB Jones. 2015. "Hydrothermal Liquefaction of Biomass: Developments from Batch to Continuous Process." *Bioresource Technology* 178:147–156.

Elliott DC, TR Hart, AJ Schmidt, GG Neuenschwander, LJ Rotness, MV Olarte, AH Zacher, KO Albrecht, RT Hallen, and JE Holladay. 2013. "Process development for hydrothermal liquefaction of algae feedstocks in a continuous-flow reactor." *Algal Research* 2:445–454.

Elliott DC, AJ Schmidt, TR Hart, and JM Billing. 2017. "Conversion of a Wet Waste Feedstock to Biocrude by Hydrothermal Processing in a Continuous-Flow Reactor: Grape Pomace." *Biomass Conversion and Biorefinery* 7:455–465.

Fernandez S, K Srinivas, AJ Schmidt, MS Swita, and BK Ahring. 2018. "Anaerobic Digestion of Organic Fraction from Hydrothermal Liquefied Algae Wastewater Byproduct." *Bioresource Technology* 247:250–258.

He Y, X Li, X Xue, MS Swita, AJ Schmidt, and B Yang. 2017. "Biological Conversion of the Aqueous Wastes from Hydrothermal Liquefaction of Algae and Pine Wood by *Rhodococci*." *Bioresource Technology* 224:457–464.

Jarvis JM, KO Albrecht, JM Billing, AJ Schmidt, RT Hallen, and TM Schaub. 2018a. "Assessment of Hydrotreatment for Hydrothermal Liquefaction Biocrudes from Sewage Sludge, Microalgae, and Pine Feedstocks." *Energy Fuels* 32:8483–8493.

Jarvis JM, JM Billing, YE Corilo, AJ Schmidt, RT Hallen, and TM Schaub. 2018b. "FT-ICR MS Analysis of Blended Pine-Microalgae Feedstock HTL Biocrudes." *Fuel* 216:341–348.

Li S, Y Jiang, LJ Snowden-Swan, JA Askander, AJ Schmidt, and JM Billing. 2021. "Techno-Economic Uncertainty Analysis of Wet Waste-to-Biocrude via Hydrothermal Liquefaction." *Applied Energy* 283:116340.

Poloski AP, RC Daniel, DR Rector, PR Bredt, EC Buck, JC Berg, and AE Sáez. 2006. *Characterization and Correlation of Particle-Level Interactions to the Macroscopic Rheology of Powders, Granular Slurries, and Colloidal Suspensions*. PNNL-16133, Pacific Northwest National Laboratory, Richland, WA, United States.

Skaggs RL, AM Coleman, TE Seiple, and AR Milbrandt. 2018. "Waste-to-Energy Biofuel Production Potential for Selected Feedstocks in the Conterminous United States." *Renewable and Sustainable Energy Review* 82:2640–2651.

Snowden-Swan LJ, JM Billing, MR Thorson, AJ Schmidt, Y Jiang, DM Santosa, TE Seiple, RC Daniel, CA Burns, S Li, TR Hart, SP Fox, MV Olarte, K Ramasamy, DB Anderson, RT Hallen, S Radovcich, PM Mathias, and MA Taylor. 2021. *Wet Waste Hydrothermal Liquefaction and Biocrude Upgrading to Hydrocarbon Fuels: 2020 State of Technology*. PNNL-30982, Pacific Northwest National Laboratory, Richland, WA, United States.

Snowden-Swan LJ, RT Hallen, Y Zhu, JM Billing, SB Jones, TR Hart, DC Elliot, SP Fox, AJ Schmidt, and GD Maupin. 2016. *Hydrothermal Liquefaction and Upgrading of Municipal Wastewater Treatment Plant Sludge: A Preliminary Techno-Economic Analysis*. PNNL-25464, Rev. 1, Pacific Northwest National Laboratory, Richland, WA, United States.

Snowden-Swan LJ, S Li, Y Jiang, MR Thorson, AJ Schmidt, TE Seiple, JM Billing, DM Santosa, TR Hart, SP Fox, DJ Cronin, K Ramasamy, DB Anderson, RT Hallen, XF Almansa, and JW Norton. 2022. *Wet Waste Hydrothermal Liquefaction and Biocrude Upgrading to Hydrocarbon Fuels: 2021 State of Technology*. PNNL-32731, Pacific Northwest National Laboratory, Richland, WA, United States.

Snowden-Swan LJ, Y Zhu, MD Bearden, TE Seiple, SB Jones, AJ Schmidt, JM Billing, RT Hallen, TR Hart, J Liu, KO Albrecht, SP Fox, GD Maupin, and DC Elliott. 2017. *Conceptual Biorefinery Design and Research Targeted for 2022: Hydrothermal Liquefaction Processing of Wet Waste to Fuels*. PNNL-27186, Pacific Northwest National Laboratory, Richland, WA, United States.

Thorson MR, DM Santosa, RT Hallen, I Kutnyakov, MV Olarte, M Flake, G Neuenschwander, L Middleton-Smith, AH Zacher, TR Hart, AJ Schmidt, T Lemmon, and M Swita. 2021. "Scaleable Hydrotreating of HTL Biocrude to Produce Fuel Blendstocks." *Energy Fuels* 35:11346–11352.

Zhu Y, MJ Biddy, SB Jones, DC Elliott, and AJ Schmidt. 2014. "Techno-economic Analysis of Liquid Fuel Production from Woody Biomass via Hydrothermal Liquefaction (HTL) and Upgrading." *Applied Energy* 129:384–394.

Zhu Y, SB Jones, AJ Schmidt, JM Billing, HM Job, JR Collett, SJ Edmundson, KR Pomraning, SP Fox, TR Hart, AE Gutknecht, PA Meyer, MR Thorson, LJ Snowden-Swan, and DB Anderson. 2021a. *Microalgae Conversion to Biofuels and Biochemical via Sequential Hydrothermal Liquefaction (SEQHTL) and Bioprocessing: 2020 State of Technology*. PNNL-30124, Pacific Northwest National Laboratory, Richland, WA, United States.

Zhu Y, SB Jones, AJ Schmidt, JM Billing, DM Santosa, and DB Anderson. 2021b. "Economic Impacts of Feeding Microalgae/Wood Blends to Hydrothermal Liquefaction and Upgrading Systems." *Algal Research* 51:102053.

Appendix A – Additional Data

In the appendix that follows, additional rheological data are provided for the five WW22 samples discussed in the main body of this report. The first set of additional data are the full three-part flow curves for each of the five samples. The second set of additional data include a full itemization of down-ramp fits to the Pseudo-Plastic and Casson constitutive equations. The third and final data set includes a full itemization of temperature sweep data and fits.

A.1 Three-Part Flow Curve Data

Three-part flow curves are reproduced on the pages that follow for the ambient, pre-treatment 25 °C, heat-treated 300 °C, and post-heat-treatment 25 °C measuring periods. Each three-part flow curve consists of an accelerating shear rate period spanning 0 to 1000 s^{-1} (the "up-ramp"), a period at which shear rate is held at 1000 s^{-1} (the "hold"), and a decelerating shear rate period spanning 1000 to 0 s^{-1} (the "down-ramp").

A.1.1 Pre-Treatment Measurement at Ambient Temperature

Flow curve data for the five WW22 samples collected at 25 °C before heat-treatment are provided in Figures A.1 to A.5 below.

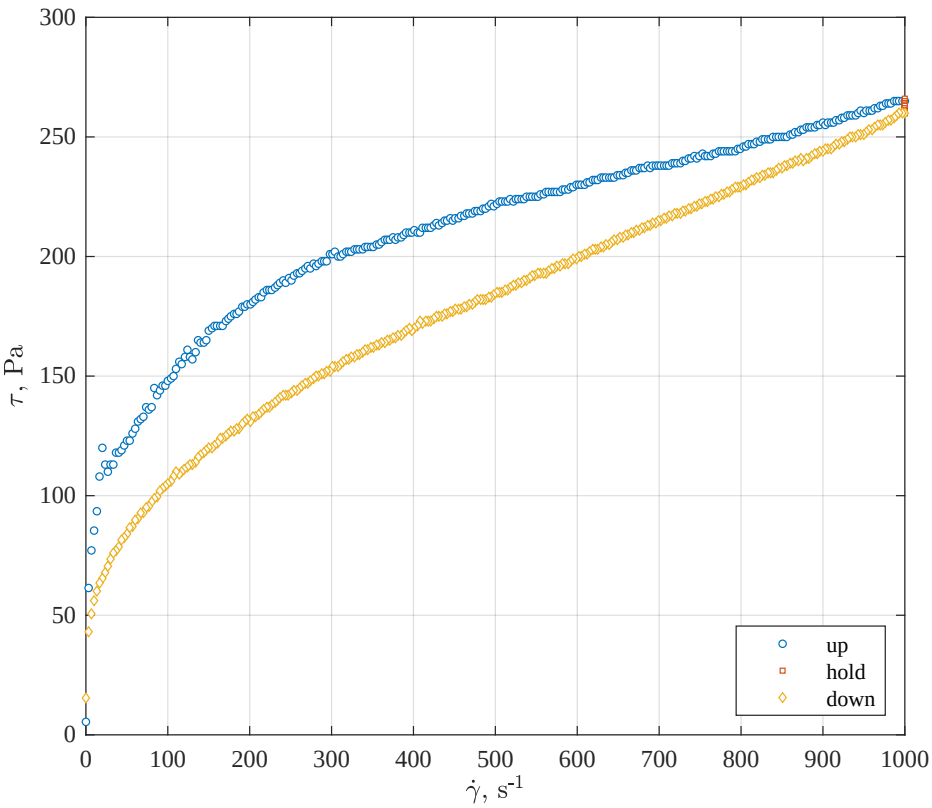

Figure A.1. Three-part flow curve for sample WW22-20-A (19.4 % solids) at 25 °C before heat treatment.

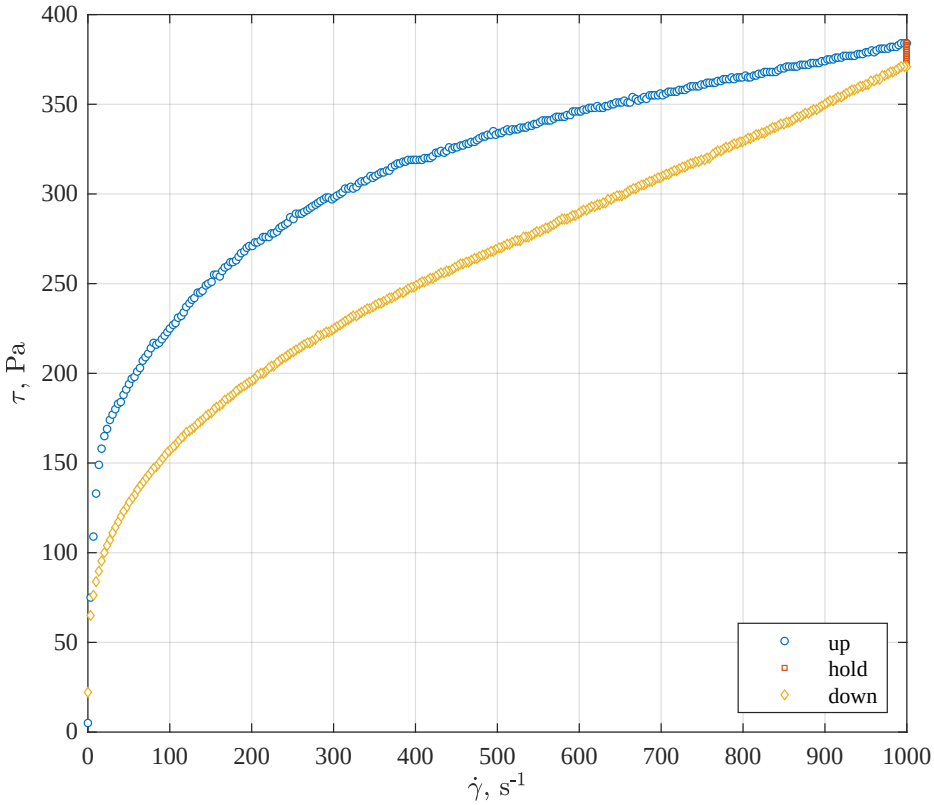

Figure A.2. Three-part flow curve for sample WW22-EOR-A (23.3 % solids) at 25 °C before heat treatment.

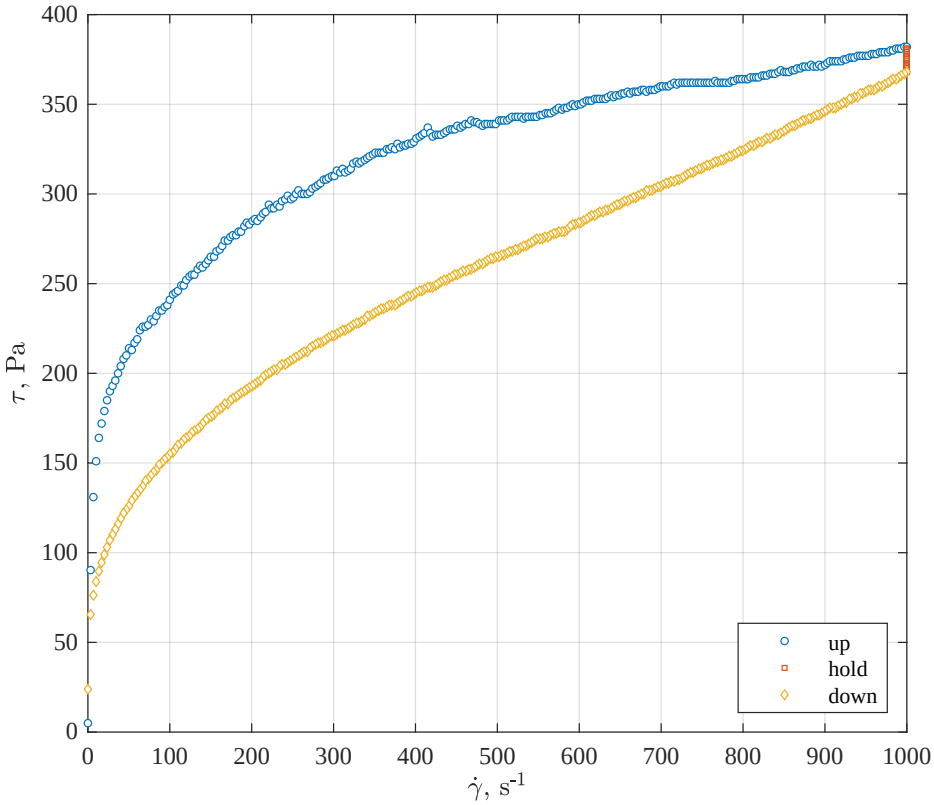

Figure A.3. Three-part flow curve for sample WW22-EOR-B (23.3 % solids) at 25 °C before heat treatment.

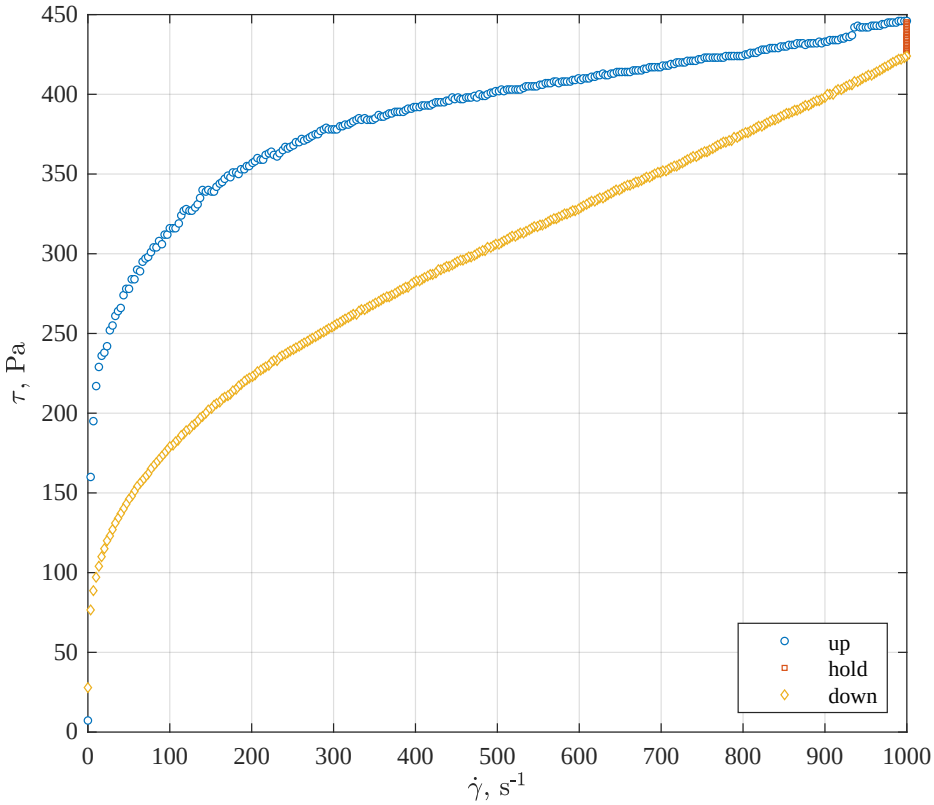

Figure A.4. Three-part flow curve for sample WW22-25-A at (24.8 % solids) 25 °C before heat treatment.

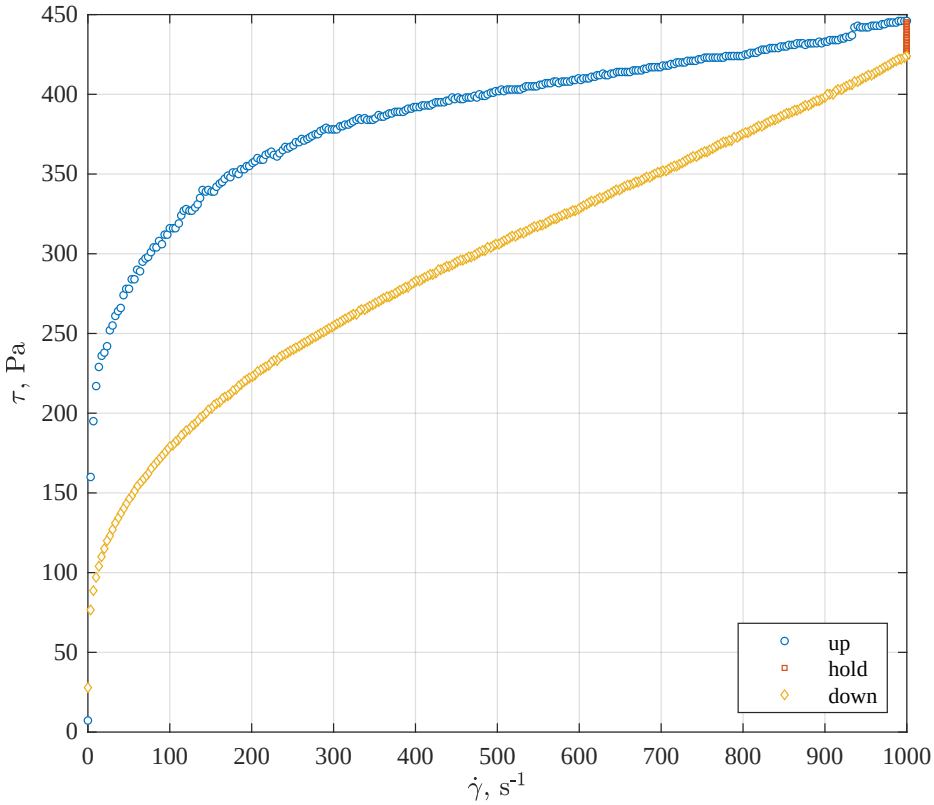

Figure A.5. Three-part flow curve for sample WW22-25-A at (24.8 % solids) 25 °C before heat treatment.

A.1.2 Post-Treatment Measurement at Elevated Temperature

Flow curve data for the five WW22 samples collected at 300 °C after heat-treatment are provided in Figures A.6 to A.10 below. The solid contents provided in each of the figure captions correspond to that measured for the samples before heat-treatment and conversion.

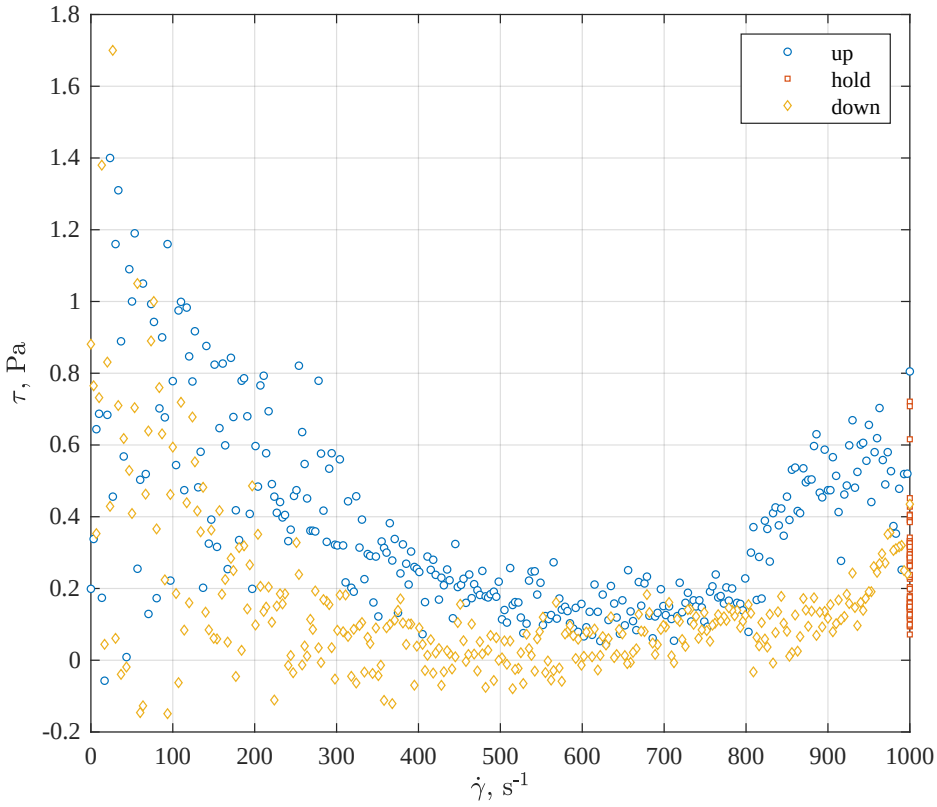

Figure A.6. Three-part flow curve for sample WW22-20-A (19.4% solids) at 300 °C after heat treatment.

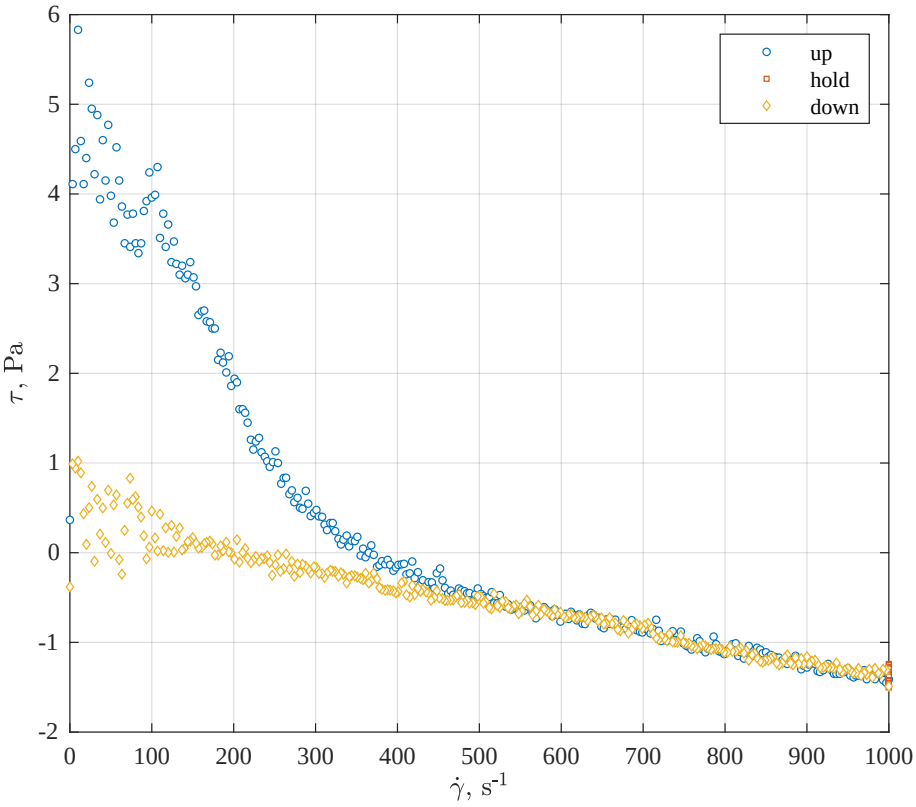

Figure A.7. Three-part flow curve for sample WW22-EOR-A (23.3 % solids) at 300 °C after heat treatment.

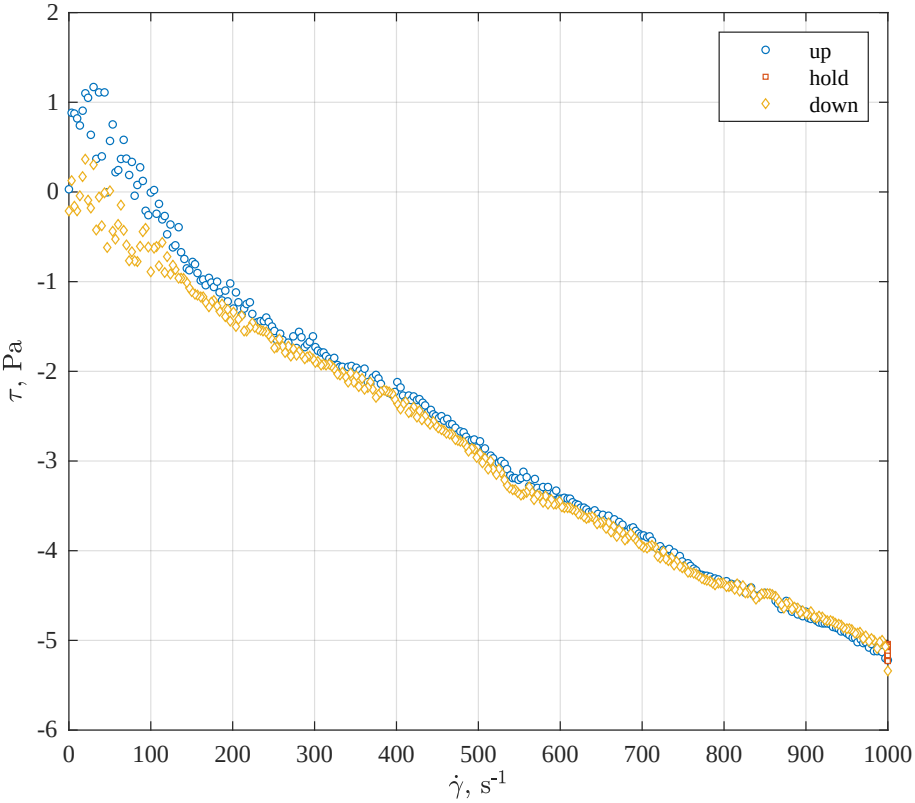

Figure A.8. Three-part flow curve for sample WW22-EOR-B (23.3 % solids) at 300 °C after heat treatment.

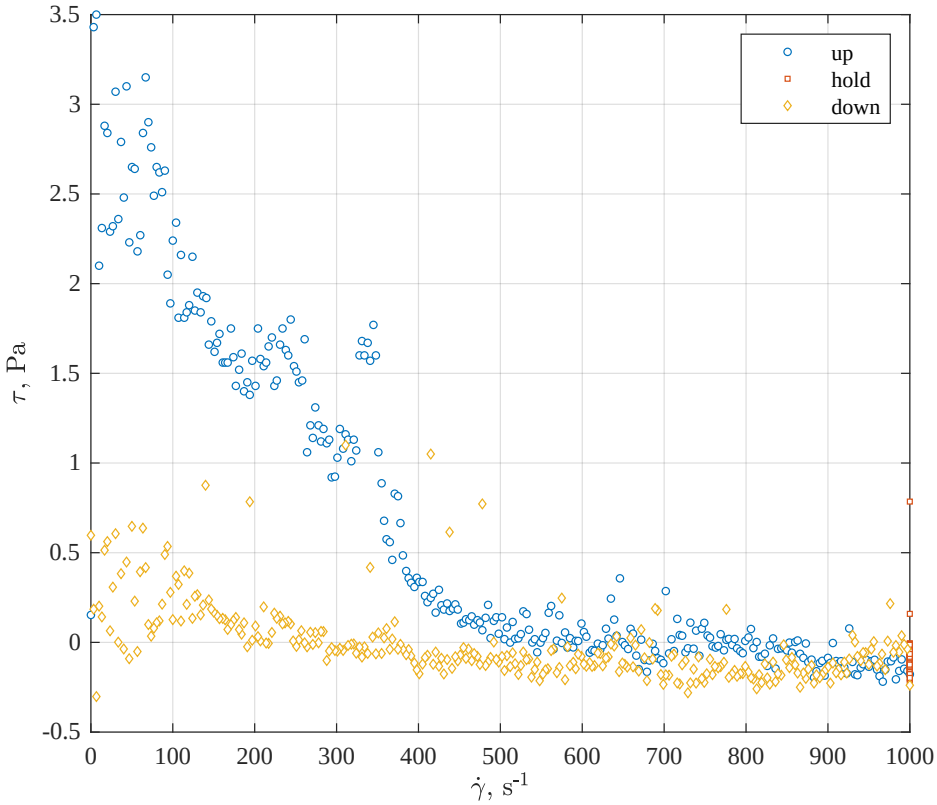

Figure A.9. Three-part flow curve for sample WW22-25-A (24.8 % solids) at 300 °C after heat treatment.

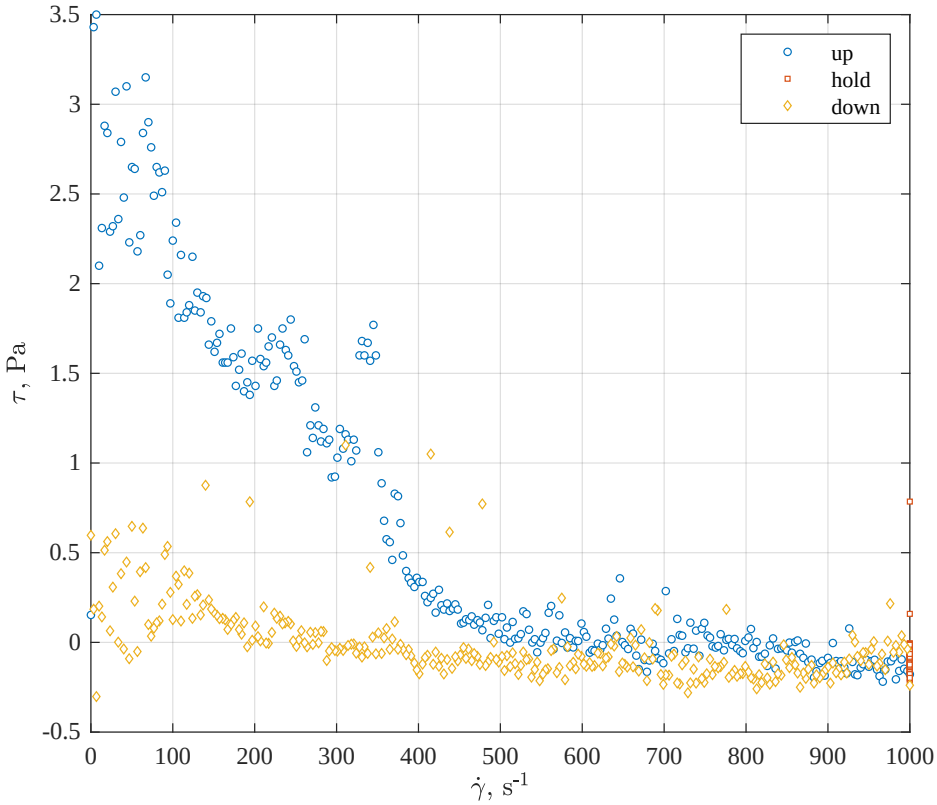

Figure A.10. Three-part flow curve for sample WW22-25-A (24.8 % solids) at 300 °C after heat treatment.

A.1.3 Post-Treatment Measurement at Ambient Temperature

Flow curve data for the five WW22 samples collected at 25 °C after heat-treatment are provided in Figures A.11 to A.15 below. The solid contents provided in each of the figure captions correspond to that measured for the samples before heat-treatment and conversion.

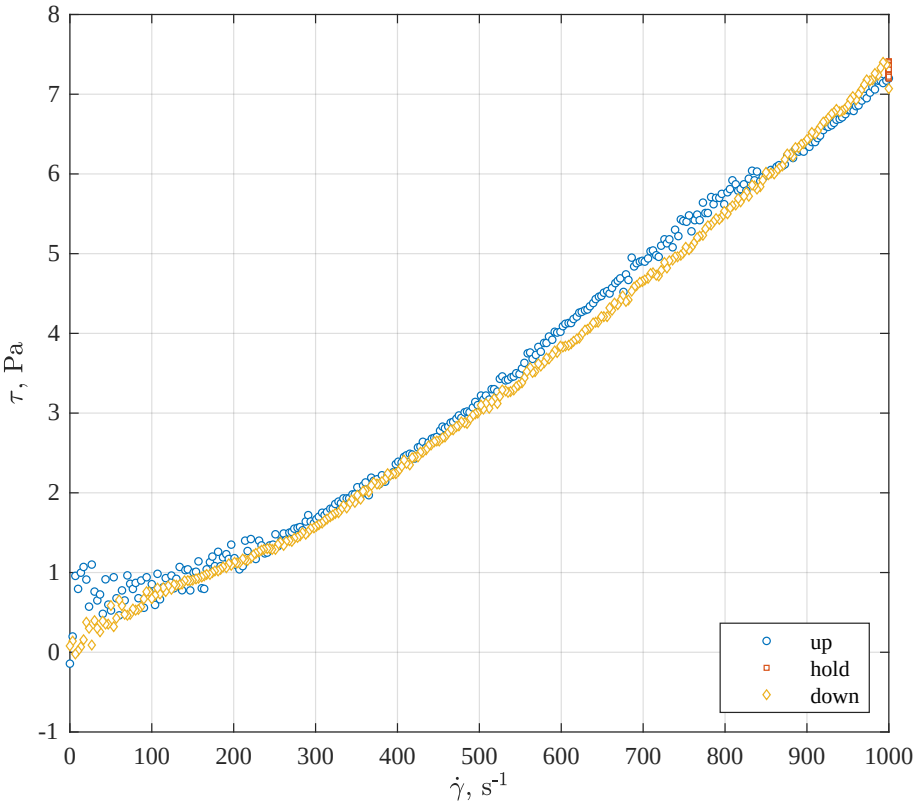

Figure A.11. Three-part flow curve for sample WW22-20-A (19.4 % solids) at 25 °C after heat treatment.

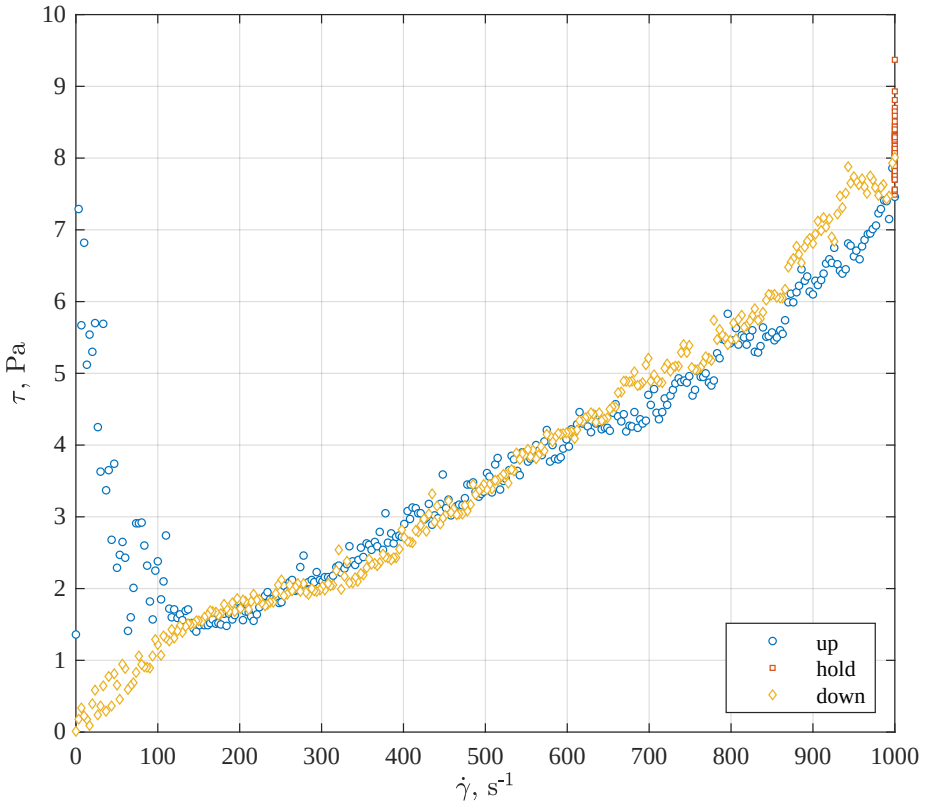

Figure A.12. Three-part flow curve for sample WW22-EOR-A (23.3 % solids) at 25 °C after heat treatment.

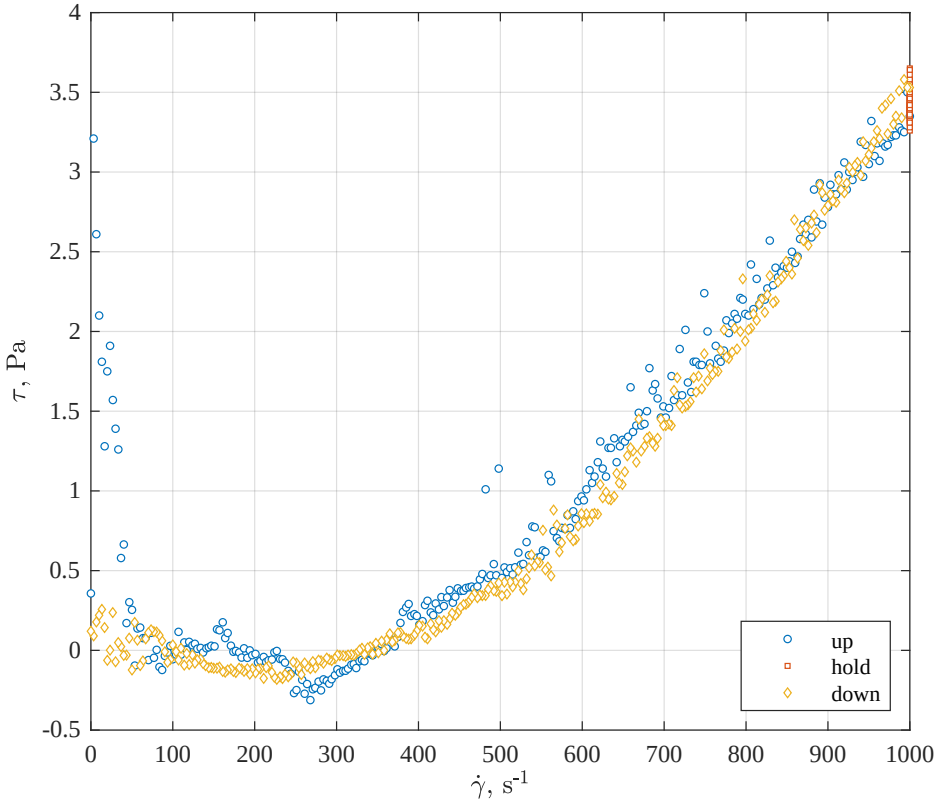

Figure A.13. Three-part flow curve for sample WW22-EOR-B (23.3 % solids) at 25 °C after heat treatment.

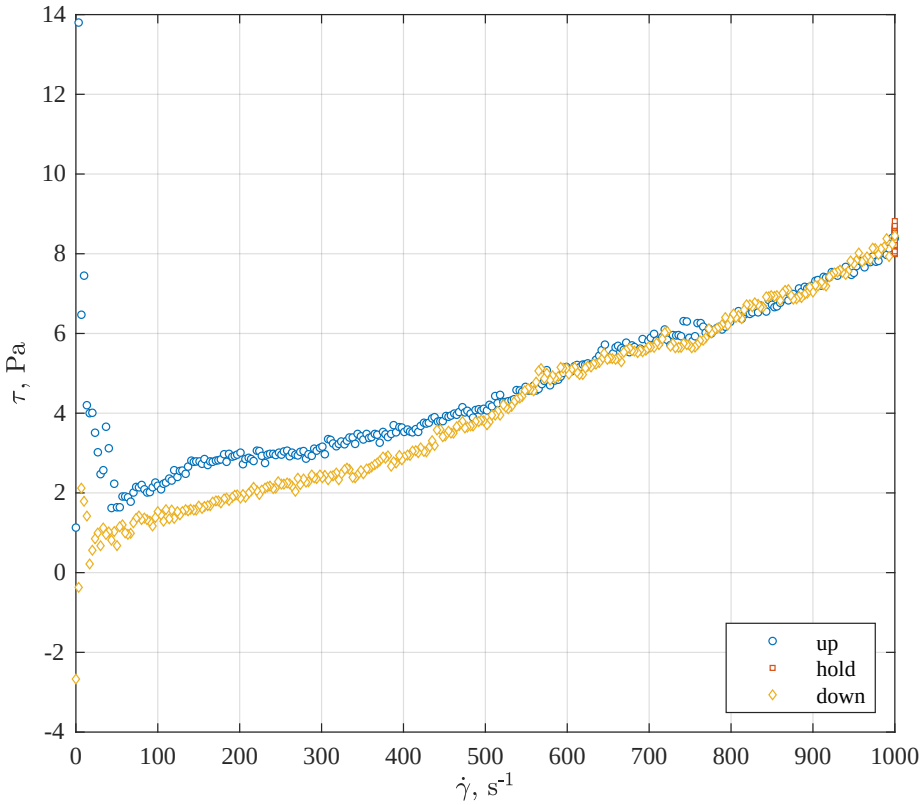

Figure A.14. Three-part flow curve for sample WW22-25-A at (24.8 % solids) 25 °C after heat treatment.

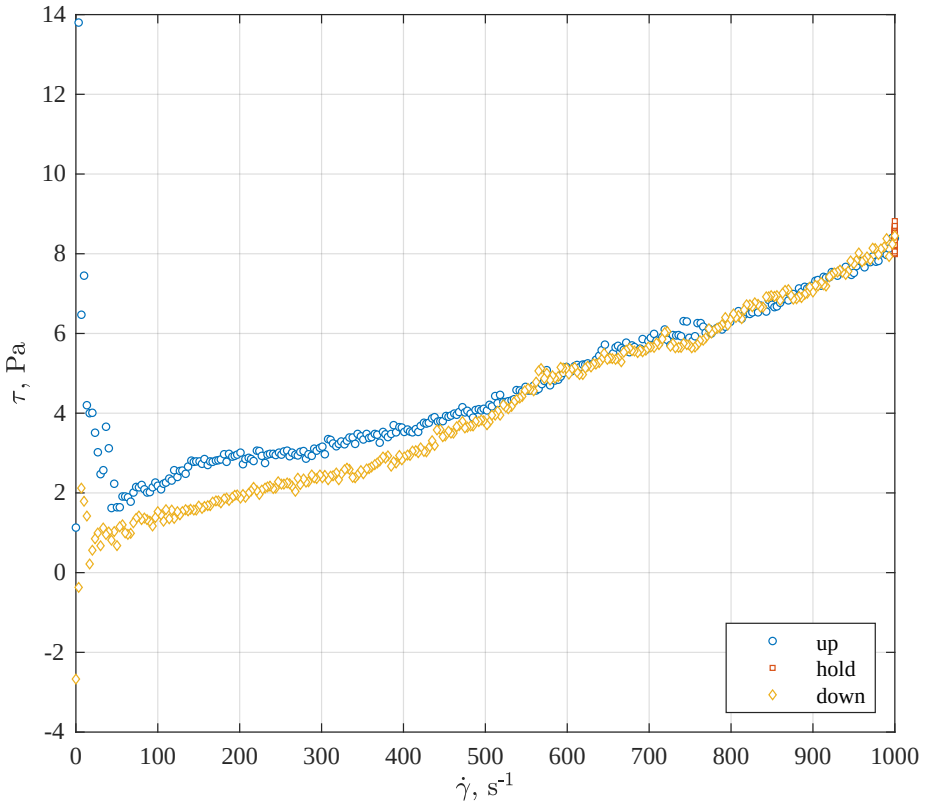

Figure A.15. Three-part flow curve for sample WW22-25-A at (24.8 % solids) 25 °C after heat treatment.

A.2 Down-Ramp Flow Curve Data and Fits

Figures A.16 through A.20 below show fits of the Pseudo-Plastic and Casson constitutive equations (Eqs. 1 and 2, respectively) to the ambient temperature (25 °C) down-ramp flow curve data for the five Feed WW22 samples. The best fit constitutive parameters are provided in Table 3 in the main body of this report.

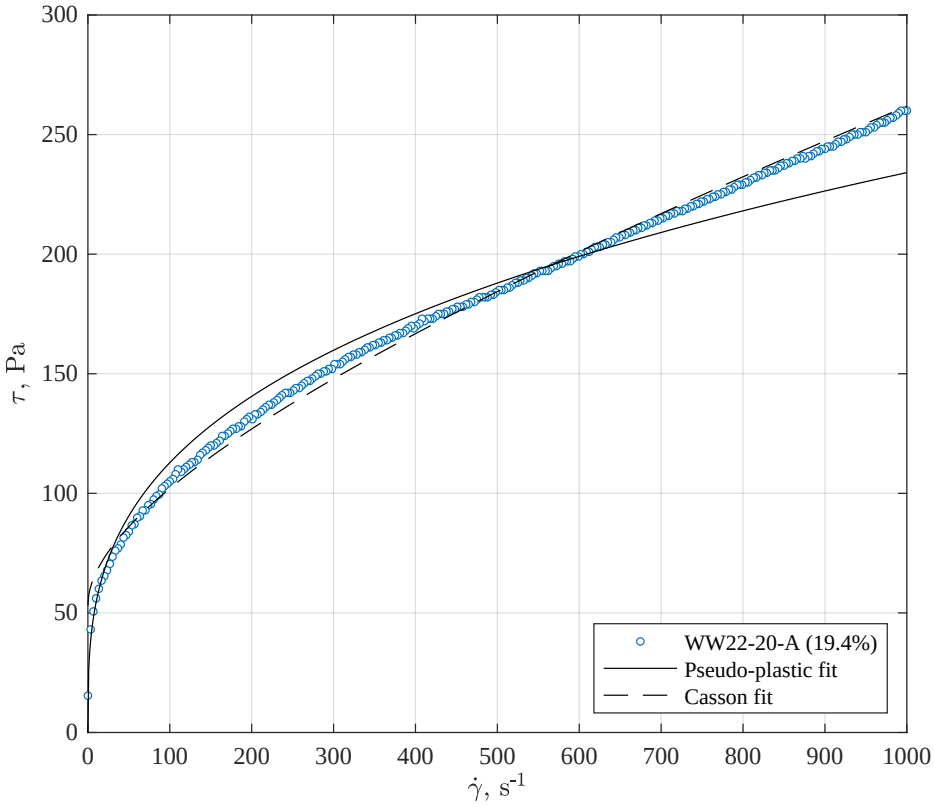

Figure A.16. Fits of the Pseudo-Plastic and Casson constitutive equations (Eqs. 1 and 2, respectively) for Sample WW22-20-A (19.4 % solids). The Sample WW22-20-A data fit corresponds to the ambient temperature (25 °C) down-ramp period before sample heat-treatment.

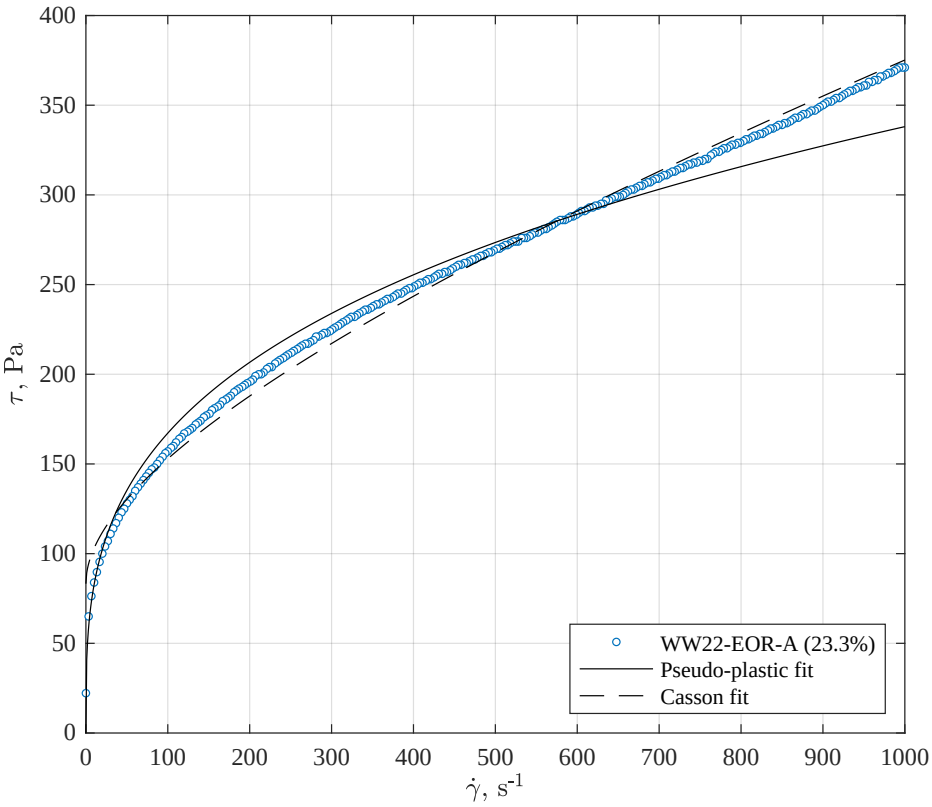

Figure A.17. Fits of the Pseudo-Plastic and Casson constitutive equations (Eqs. 1 and 2, respectively) for Sample WW22-EOR-A (23.3 % solids). The Sample WW22-EOR-A data fit corresponds to the ambient temperature (25 °C) down-ramp period before sample heat-treatment.

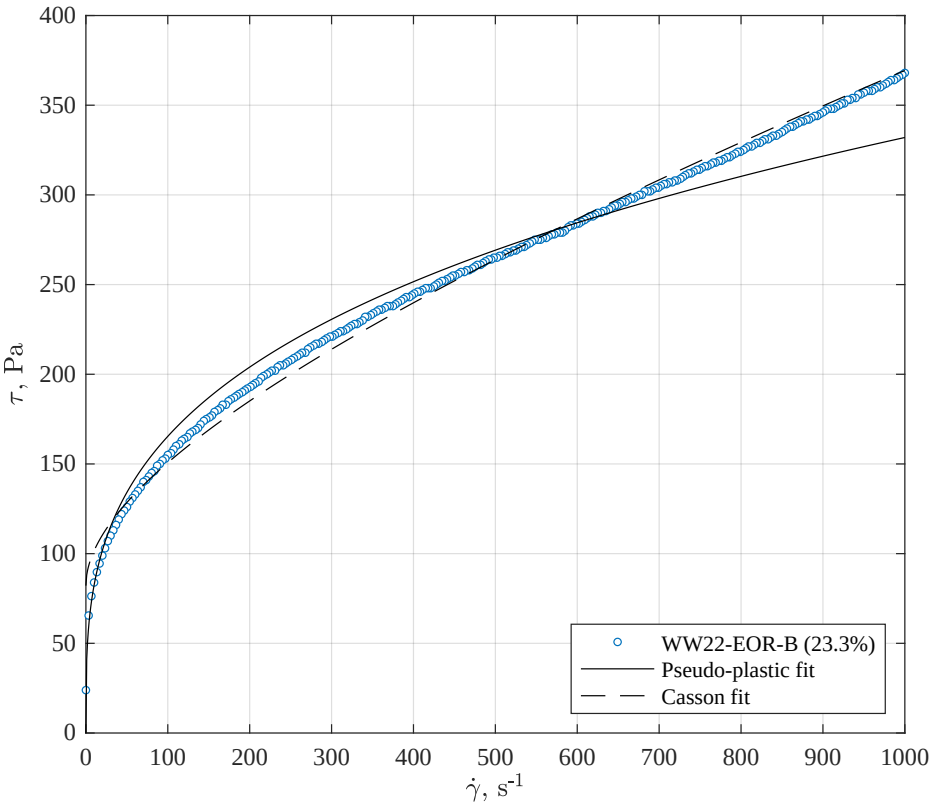

Figure A.18. Fits of the Pseudo-Plastic and Casson constitutive equations (Eqs. 1 and 2, respectively) for Sample WW22-EOR-B (23.3 % solids). The Sample WW22-EOR-B data fit corresponds to the ambient temperature (25 °C) down-ramp period before sample heat-treatment.

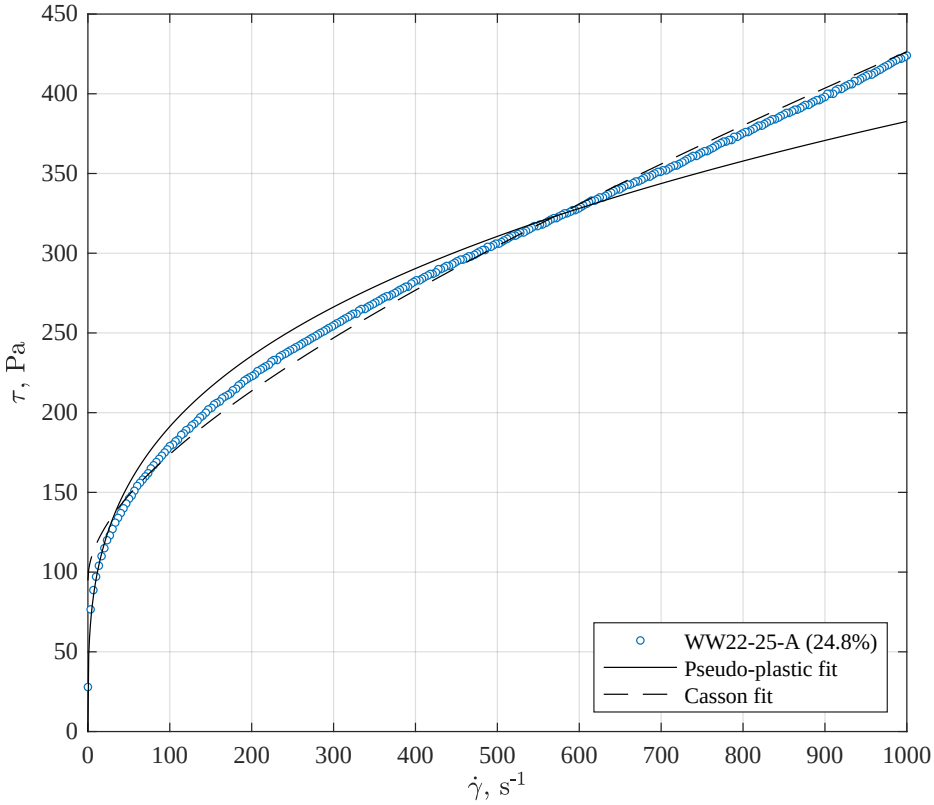

Figure A.19. Fits of the Pseudo-Plastic and Casson constitutive equations (Eqs. 1 and 2, respectively) for Sample WW22-25-A (24.8 % solids). The Sample WW22-25-A data fit corresponds to the ambient temperature (25 °C) down-ramp period before sample heat-treatment.

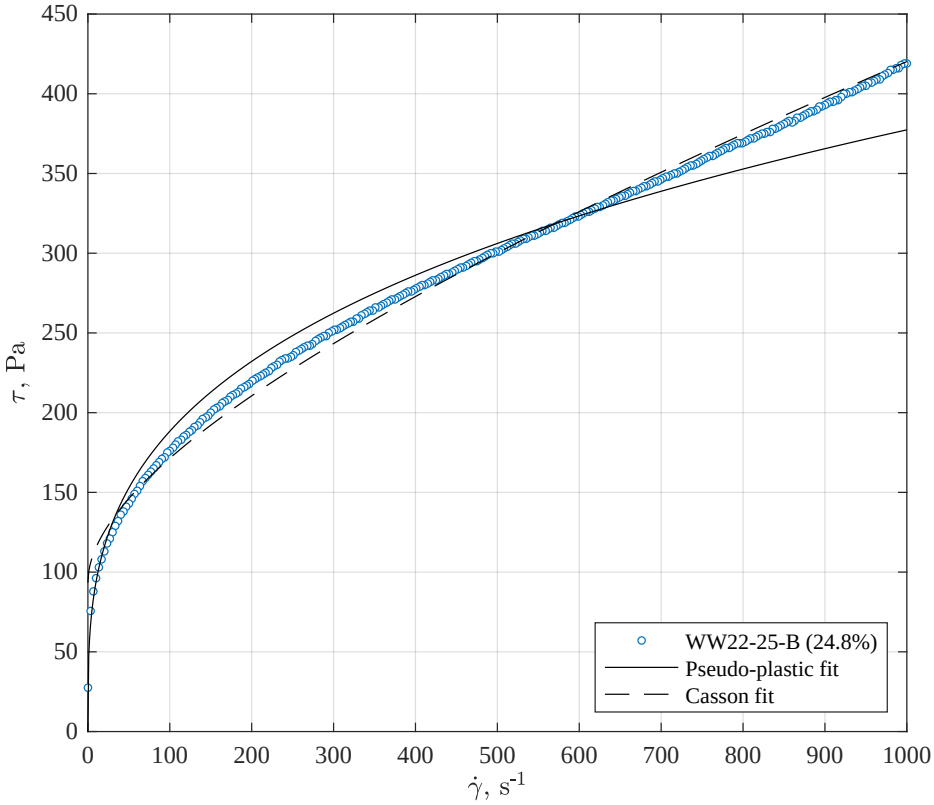

Figure A.20. Fits of the Pseudo-Plastic and Casson constitutive equations (Eqs. 1 and 2, respectively) for Sample WW22-25-B (24.8 % solids). The Sample WW22-25-B data fit corresponds to the ambient temperature (25 °C) down-ramp period before sample heat-treatment.

A.3 Temperature Sweep Data and Fits

Figures A.21 through A.25 below show fits of the simple temperature model (Eq. 4) to the 25 to 300 °C temperature sweep data collected for the five Feed WW22 samples. The best fit temperature sweep parameters are provided in Table 4 in the main body of this report.

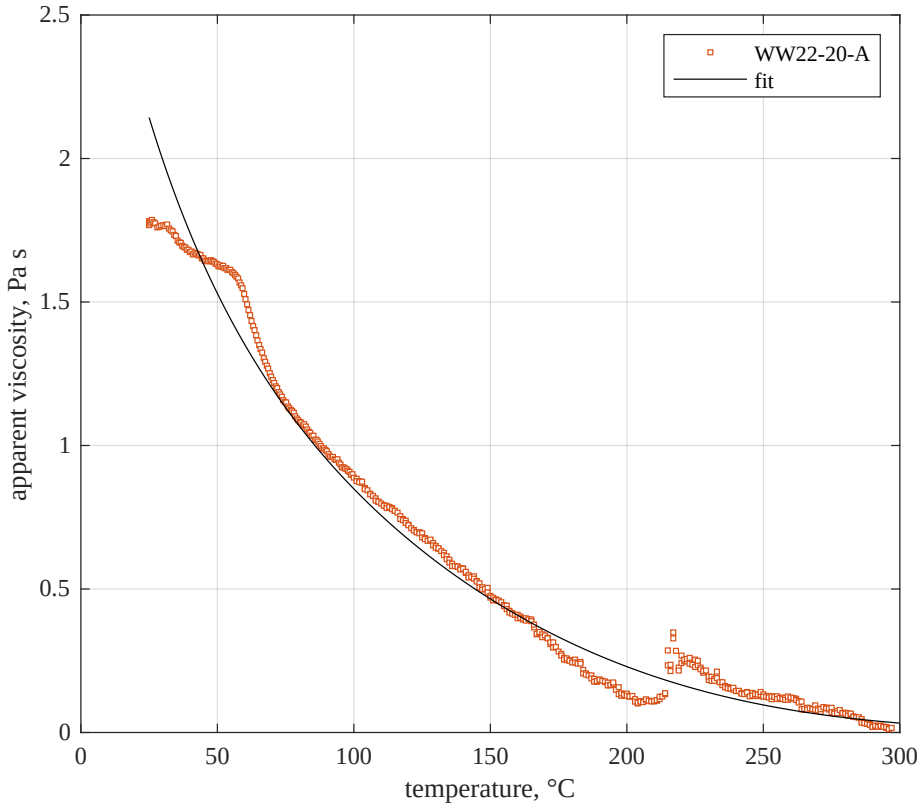

Figure A.21. Fit of the simple temperature sweep model (Eq. 4) for Sample WW22-20-A ($\dot{\gamma} = 50\,\mathrm{s}^{-1}$). The Sample WW22-20-A data fit corresponds to the 25 to 300 °C sample temperature sweep period. Sample WW22-20-A had a solids content of 19.4 % (by mass) before heat treatment and conversion.

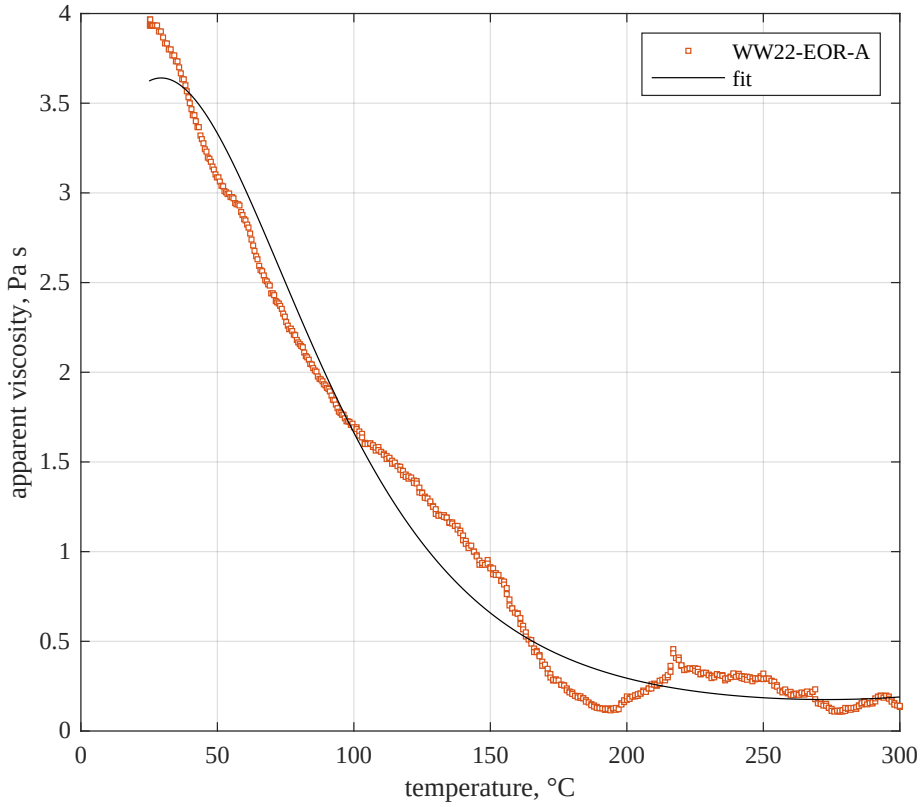

Figure A.22. Fit of the simple temperature sweep model (Eq. 4) for Sample WW22-EOR-A ($\dot{\gamma} = 30\,\mathrm{s}^{-1}$). The Sample WW22-EOR-A data fit corresponds to the 25 to 300 °C sample temperature sweep period. Sample WW22-EOR-A had a solids content of 23.3% (by mass) before heat treatment and conversion.

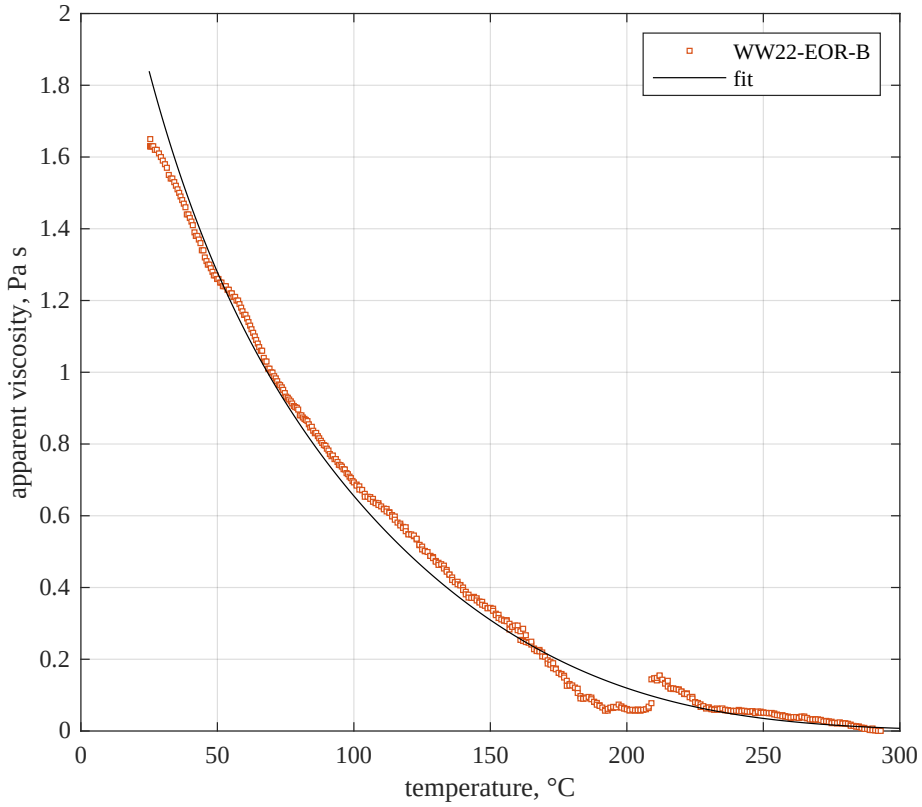

Figure A.23. Fit of the simple temperature sweep model (Eq. 4) for Sample WW22-EOR-B ($\dot{\gamma} = 100\,\mathrm{s}^{-1}$). The Sample WW22-EOR-B data fit corresponds to the 25 to 300 °C sample temperature sweep period. Sample WW22-EOR-B had a solids content of 23.3 % (by mass) before heat treatment and conversion.

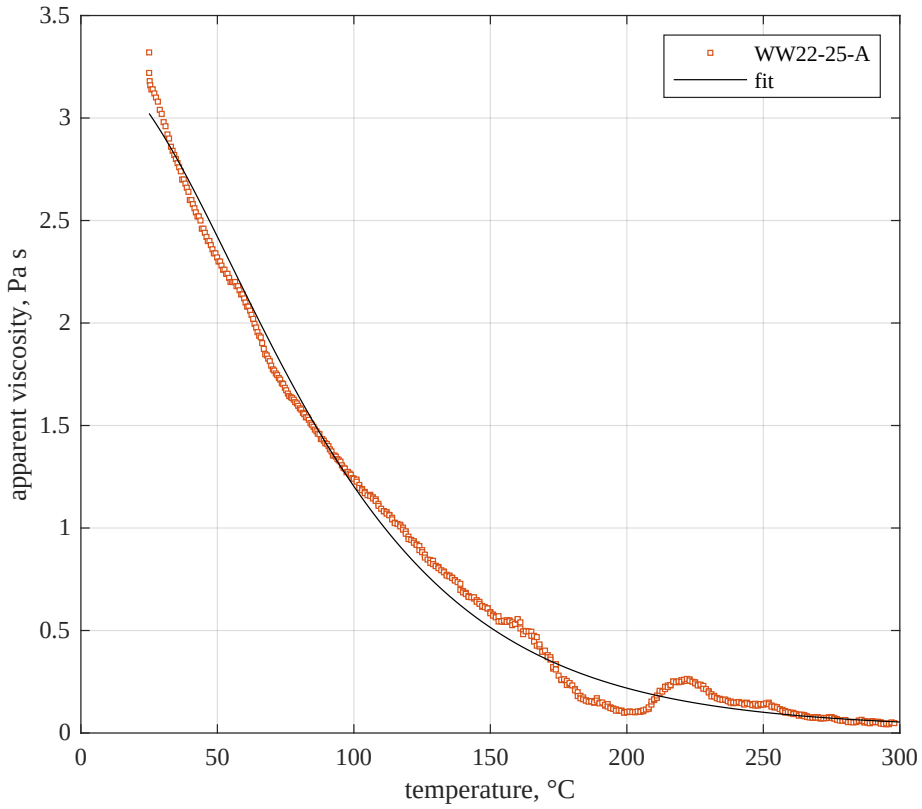

Figure A.24. Fit of the simple temperature sweep model (Eq. 4) for Sample WW22-25-A ($\dot{\gamma} = 50\,\mathrm{s}^{-1}$). The Sample WW22-25-A data fit corresponds to the 25 to 300 °C sample temperature sweep period. Sample WW22-25-A had a solids content of 24.8 % (by mass) before heat treatment and conversion.

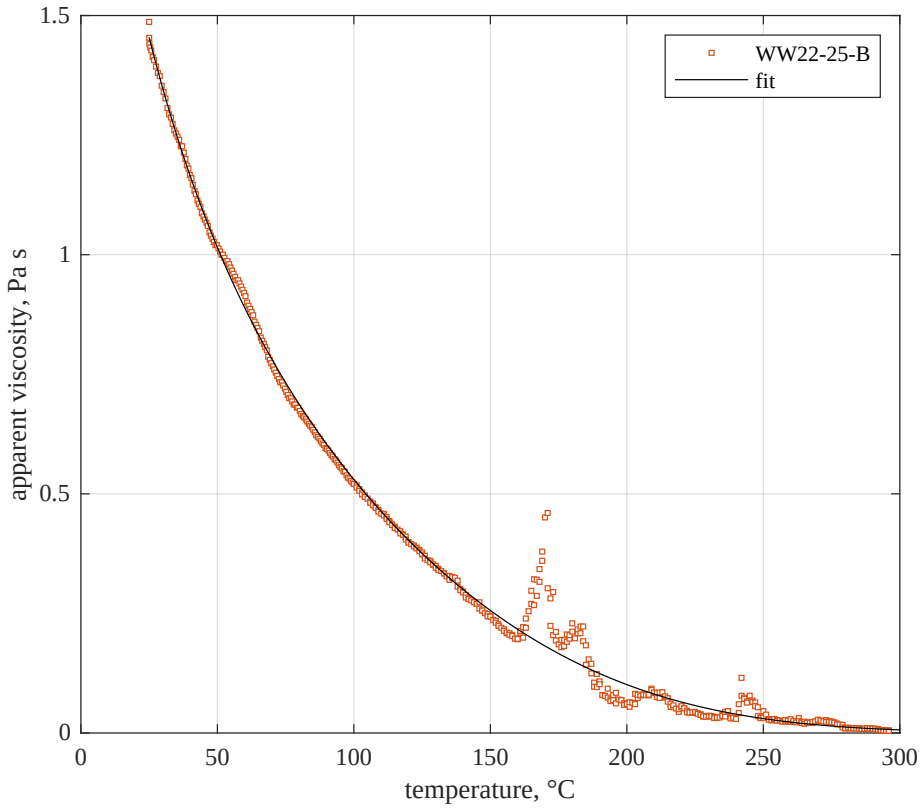

Figure A.25. Fit of the simple temperature sweep model (Eq. 4) for Sample WW22-25-B ($\dot{\gamma} = 150\,\mathrm{s}^{-1}$). The Sample WW22-25-B data fit corresponds to the 25 to 300 °C sample temperature sweep period. Sample WW22-25-B had a solids content of 24.8 % (by mass) before heat treatment and conversion.

Pacific Northwest National Laboratory

902 Battelle Boulevard
P.O. Box 999
Richland, WA 99352
1-888-375-PNNL (7675)

www.pnnl.gov